Machinability study on GCI brake discs

Effects of material variations and

process behavior on tool life

Christian Jaunviksna

2023

Abstract

Grey cast iron is one of the most used materials in the automotive industry. The material has a range of properties that makes it suitable for machining applications, but manufacturers still experience machinability problems. Automotive Components Floby (ACF), who currently experience machinability issues with brake discs, initiated this study to gain further understanding of tool deterioration in machining of grey cast iron. They provided two brake discs with known relative machinability for the experiments. Machining tests were performed where dynamic cutting forces were recorded, and chip segments were collected. Hardness measurements with nano indentation and SEM microscopy for structure analysis were also performed. The cutting forces and hardness values were analyzed statistically to get representative models for the results.

The cutting force analyses showed that a high segmentation frequency is desirable for improved machinability. The deformed geometry of the chip segments showed that the material with bad machinability had to travel longer into the workpiece to produce one chip segment. This confirms that a high segmentation frequency is desired.

The relation of the feed force and the main cutting force also showed to be of importance. A low feed force compared to the main cutting force reduces the contact surface on the inserts flank face, which improves machinability.

The relative hardness between the materials showed that high hardness in general, and high pearlitic hardness in particular are desirable properties. This holds if the cutting tool is harder than the workpiece matrix and its inclusions.

The microstructure analysis gave some unexpected results. It showed that the hardest inclusions were found in the material with good machinability. It also showed that presence of steadite could help with chip breaking, improving machinability. This holds as long as the tool material is harder than the hard steadite. More expected results were that machinability was improved by a uniform graphite structure and small grain size.

Worn cutting tools were collected from the production line at ACF. These were analyzed under microscope to clarify the wear problems at hand. The results showed abrasive wear, chemical wear and adhesion of workpiece material to the cutting edge. It was assumed that the wear problems were in part cutting data related, so attempts to suggest development paths for ACF were made. The suggestions were based on a literature survey, and although promising examples of cutting data optimization were found, no real confident proposals could be done. Their machinability issues are experienced on a batch-to-batch basis, which indicates that each batch needs a unique set of cutting data. That is hard to accomplish, as long as the company does not have the ability to analyze each batch in house.

Preface

This master's thesis is a part of the project *Sustainable production realization of cast iron components in an extended value chain (2019-03118),* financed by Vinnova. The project was initiated to reduce environmental impacts due to downtimes and discarded material when machining grey cast iron.

The project was performed in collaboration with Automotive Components Floby and the Division of Production and Materials Engineering at Lund University, during the time period from September 2022 to January 2023. Some of the work was performed at AC Flobys facilities in Floby, but the main part of the project's experiments and analyses were carried out at the Division of Production and Materials Engineering in Lund.

The process of writing this thesis has been a learning and humbling experience. It would not have been possible to complete it on my own. I want to express my sincere gratitude to the following people:

Jan-Eric Ståhl	The meetings with you and your extensive bibliography have made the incomprehensible comprehensible. I have learned a lot, thank you!
Christina Windmark	Thank you for initiating the project and the contact with AC Floby.
Samuel Awe	Your guidance and feedback through several stages of the project was very encouraging, thank you!
Rebecka Lindvall	Your guidance and all the hours you spent with me by the SEM will not be forgotten.
Jinming Zhou	I really appreciate the time and effort you put into recording the extensive hardness data.
Juan Manuel Bello Bermejo	Thank you for the cooperation when we tried to wrap our heads around the statistical analysis.
Parsa Rostami	Thank you for your assistance in the preparation and execution of the cutting force measurements. And for your effort in the statistical analysis.

Table Of Contents

Nomenclature, symbols, and abbreviations

A list of symbols and abbreviations, together with their units is presented below.

Symbol	Meaning	Unit
a_p	Cutting depth	mm
ACF	Automotive Components Floby	-
B_1	Bad machinability, direction 1	-
B_2	Bad machinability, direction 2	-
B_3	Bad machinability, direction 3	-
BM	Disc with bad machinability	-
BUE	Built-up edge	-
BUL	Built-up layer	-
cBN	Cubic boron nitride	-
CDF	Cumulative distribution function	-
e_1	Segmentation distance	mm
e_2	Deformed segmentation distance	mm
f	Feed rate	mm/rev
F_c	Main cutting force	N
F_f	Feed force	N
F_p	Passive force	N
G_1	Good machinability, direction 1	-
G_2	Good machinability, direction 2	-
G_3	Good machinability, direction 3	-
GCI	Grey cast iron	-
GM	Disc with good machinability	-
h_1	Theoretical chip thickness	mm
h_2	Deformed chip thickness	mm
l_c	Contact length	μm
MRR	Material removal rate	cm^3/min

pcBN	Polycrystalline cubic boron nitride	-
PDF	Probability density function	-
SEM	Scanning Electron Microscope	-
v_c	Cutting speed	m/min
XEDS	Energy-dispersive X-ray spectroscopy	-
κ	Major cutting angle	°
φ_{AT}	Load function in the AT-plane	-

1 Introduction

Grey cast iron (GCI) is a material commonly used in brake rotor applications. Due to its desirable machining properties and beneficial price point, it is one of the most used materials in the automotive industry. The casting industry is however changing. For example, cost reduction and environmental concerns has led to an increased amount of recycled materials in the castings supplied by the foundries. This can lead to problems with unwanted impurities and trace elements, affecting tool life and surface quality in the machining process. Measures to analyze workpiece materials and their machinability are therefore necessary [1].

Automotive Components Floby (ACF) produces connecting rods, wheel hubs and brake discs for both personal and commercial vehicles. They are currently experiencing problems with several of their brake discs, and machinability varies on a batch-to-batch basis. This leads to excessive tool wear and poor surface quality of the products. Before the discs are machined, they are stored for at least 14 days. This is done to make sure that the main portion of natural ageing has taken place in the material, to improve machinability. Still, production costs and downtimes increase due to frequent tool changes. A decrease of 60% and 91% in expected lifespan for rough and fine turning inserts respectively has been documented. This has led to the scrapping of about 5-15% of the GCI brake discs machined.

This study will observe two materials with known relative machinability. ACF has provided one brake disc with documented bad machinability, and one with reasonably good machinability. These discs will be turned while data of dynamic cutting forces will be collected. Process behavior will be linked to hardness and microstructure to see how each parameter might affect the machinability. In addition, worn inserts will be collected from the production line at ACF to identify the wear mechanisms causing the problems at hand.

1.1 Objectives

The purpose of this study is to gain further understanding of tool deterioration in machining of GCI. This will be done by connecting process behavior, material hardness and microstructural properties by observing turning operations of GCI brake discs. The objectives can be described by the following questions.

- Q1. Which tool wear mechanisms are predominant in turning of GCI brake discs?
- Q2. How do material variations and process behavior influence machinability?
- Q3. Are there any development paths to optimize cutting data in terms of economy and machinability?

1.2 Limitations

During the project, micro hardness was analyzed in three directions of each material. This was done in the bulk of the material. It would have been desirable to also analyze the materials closer to the surface. Due to time constraints within the project, this was disregarded.

When comparing the hardness to the microstructure, it would have been appropriate to analyze the structure in each respective direction. This too was disregarded due to time constraints, and the structure was only analyzed in the direction of the main cutting forces.

2 Theory

This chapter presents the theory necessary to understand the project. The report is written in a manner so a reader with limited knowledge in machining can follow along.

2.1 Turning

Turning is a machining operation where a single cutting edge is engaged with a rotating workpiece. The workpiece is secured in a chuck, while the tool is rigidly held in a tool post. The tool moves at a constant speed, either perpendicular to, or along the axis that the workpiece is rotating around. For each predefined path, the tool cuts away chips of metal to obtain the desired geometry of the workpiece [2]. The turning process can be described by the directions and planes that are involved. The directions are the tangential, the radial, and the axial directions. They are illustrated in *Figure 1* below, abbreviated as *T*, *A*, and *R*. Combinations of these directions make up the planes of the of the process, also found in *Figure 1* [3].
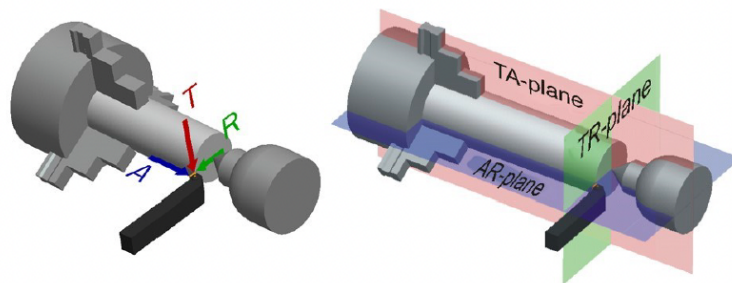

Figure 1. Planes and directions of turning operation [3].

2.1.1 Cutting data

The most crucial data to optimize in a turning operation are the cutting speed v_c, the feed f, and the depth of cut a_p. The cutting speed is the relative speed between the edge of the tool and the surface of the workpiece, expressed in m/min [2]. The feed is the movement of the tool. The movement could be either axial or radial and is expressed in mm/rev. The cutting depth is the distance, perpendicular to the feed direction, that the tool is fed into the workpiece [3]. The cutting data are related to the cutting forces in such a manner that the forces increase with higher values of feed and depth of cut, and they decrease with increased cutting speed and elevated temperatures [4]. The feed and the cutting depth are illustrated in *Figure 2*.

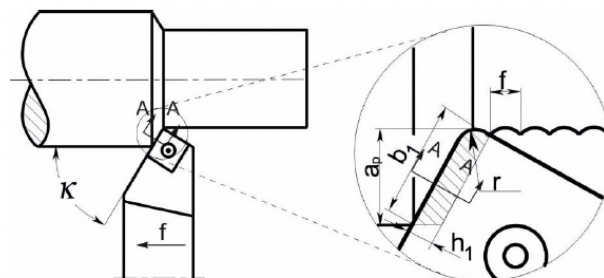*Figure 2. Major chip area parameters for turning, shown in the AR-plane [3].*

The cutting data combined determines the material removal rate *MRR*, also referred to as chip volume removed per unit time [3]. The *MRR* is given in *Equation 1* below.

$$MRR = a_p \, f \, v_c$$ *Equation 1*

The theoretical chip thickness h_1 can be derived from *Figure 2*, which results in *Equation 2*.

$$h_1 = f sin(\kappa)$$ *Equation 2*

2.1.2 Cutting forces

Figure 3 shows the cutting force and its three orthogonal components. The components are divided into a main cutting force F_c, a feed force F_f and a passive force F_p [1].
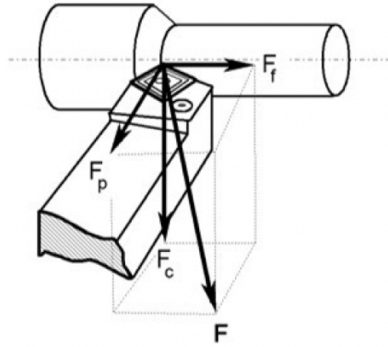

Figure 3. Cutting forces during turning operation [3].

The geometry in *Figure 3* proposes the relation between the cutting force and its components found in *Equation 3* below.

Equation 3
$$F = \sqrt{F_c^2 + F_f^2 + F_p^2}$$

2.1.2.2 Dynamic cutting forces

Cutting forces can be described by either their static or dynamic characteristics. When observing static cutting forces, an average value is measured over time. Most cutting processes do however have a dynamic nature, where a lot can be learned from the amplitudes and frequencies of the process. The amplitude of a dynamic cutting force can be described by the variation factor ψ, which is a measure of the proportional deviation in amplitude from the static cutting force in a given moment in time. This description is clarified by *Equation 4* below [1].

Equation 4
$$\psi_c(t) = \frac{F_c(t) - F_c}{F_c} = \frac{F_c(t)}{F_c} - 1$$

The dynamic behavior of the cutting process is in essence a result of chip formation, i.e., the oscillations of the main cutting force indicate what occurs on the rake face (see *Figure 5*) of the tool. This is verified by experimental data that show a decreasing variation factor when the chip thickness is reduced. When the chip thickness approaches zero, the cutting forces behave close to static [1].

2.1.2.2.1 Load functions

To describe the proportional load distribution on the tool's major flank face (see *Figure 5*), one can use a load function that shows the relation between the feed force and main cutting force. It is found in *Equation 5* below, and indices of A and T refers to the directions from *Figure 1* [1].

$$\varphi_{AT} = \frac{F_f}{F_c}$$
Equation 5

Studies have shown that a high value of φ_{AT} generates a high load on the clearance face. This indicates a large contact surface between the tool flank and the workpiece. The contact surface is the product of the engagement length along the cutting edge (b_l in *Figure 2*), and the contact length l_c on the clearance face, perpendicular to the cutting edge [5]. In machining, a short contact length is desired. This will decrease the feed forces and the chip thickness, affecting segmentation, process temperature and overall power consumption. This can be achieved by for example increasing the clearance angle [2].

2.1.2.2.2 Fourier transform

In signal analysis, Fourier transform is a central concept. It enables collected data to be represented in different domains. If force measurement data is collected in the time domain, one can use Fourier transform to convert the data to be represented in the frequency domain. This has proven to be useful in several applications [6]. A signal can be expressed both in the frequency and the time domain according to the equations below.

$$X(f) = \int_{-\infty}^{\infty} x(t)e^{-i\cdot 2\pi ft}dt$$
Equation 6

$$x(t) = \int_{-\infty}^{\infty} X(f)e^{i\cdot 2\pi ft}df$$
Equation 7

Using Perceval's theorem, i.e., that the sum or integral of the square of a function is equal to the sum or integral of the square of its transform, one obtains *Equation 8*.

$$\int_{-\infty}^{\infty} |x(t)|^2\, dt = \int_{-\infty}^{\infty} |X(f)|^2 df$$
Equation 8

Experimental frequency analysis has discrete signals, limited by the sampling frequency. By rewriting *Equation 6*, adapting it to discrete analysis, one obtains the Discrete Fourier transform presented in *Equation 9* below [6].

$$X(k) = \sum_{n=0}^{N-1} x(n)e^{-i\cdot 2\pi kn/N}$$
Equation 9

The expression above can be used to express the relative amplitudes of a signal in the frequency domain. This enables frequency analysis of cutting forces recorded as a function of time. *Figure 4* illustrates the process of the Fourier transform.
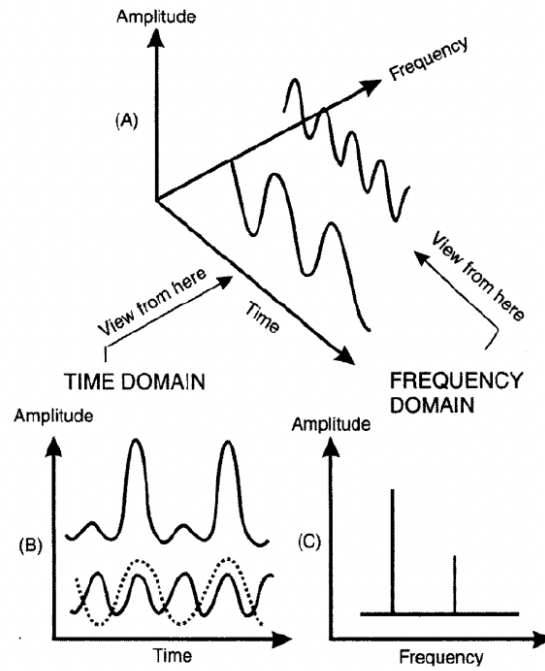
Figure 4. Illustration of a data set presented in both the time and frequency domain [7].

2.2 Cutting tools

A modern metal cutting tool consists of an insert clamped onto a tool holder which is mounted on the lathe. The surfaces of the insert are depicted in **Figure 5**.
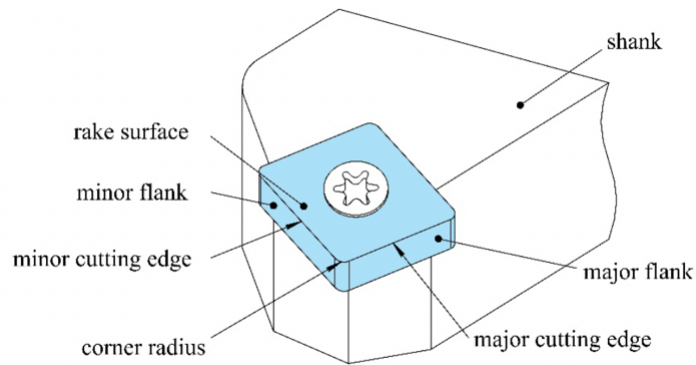

Figure 5. Schematic illustration of the surfaces on an insert [8].

2.2.1 Geometry

The designation of an insert reveals a lot about its geometry. An insert could for example be designated SCGN 090408. Here S constitutes the shape of the insert, C is the clearance angle (illustrated in *Figure 7*), G is the tolerance class, and N constitutes the chip breaker geometry. 09 is the length of the cutting edge, 04 is the insert thickness and the 08 is the nose radius (illustrated in *Figure* 7) in tenths of mm. The length and thickness are expressed in mm, and information about letter designation can be found in the tables exemplified in *Figure 6*.

Some tool geometry is dependent on the insert's attachment to the tool holder and the machine [1]. This is illustrated in *Figure 7* below.

Insert shape		Normal clearance angle α_n	
V	35°		
D	55°		
E	75°		
C	80°		
M	86°	N	0°
K	55°	A	3°
B	82°	B	5°
A	85°	C	7°
R		P	11°
S	90°	D	15°
T	60°	E	20°
W	80°	F	25°
L		G	30°
P	108°		
H	120°	O	Clearance angle which requires special data.
O	135°		

Figure 6. Tabulated values of tool geometry designations [9].

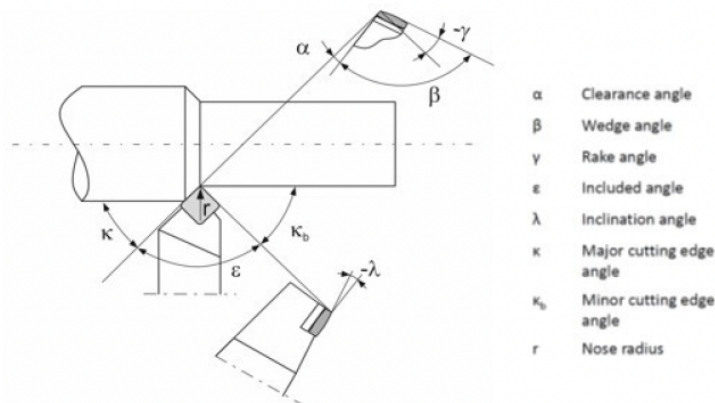|	
α	Clearance angle
β	Wedge angle
γ	Rake angle
ε	Included angle
λ	Inclination angle
κ	Major cutting edge angle
κ_b	Minor cutting edge angle
r	Nose radius

Figure 7. Geometry of turning operation [3].

2.2.2 Compositions

A wide range of material combinations and techniques can be used to produce cutting tools. In the subsequent sections, cutting tool compositions used within this project are explained.

2.2.2.1 Cemented carbide

Cemented carbides contitutes a group of composite materials with high wear resistance and high levels of hardness and strength. They are manufactured with powder metallurgy techniques, where hard particles are sintered together by a tough binder material. Tungsten carbide (WC) is the most common hard phase, while cobalt has become the most used binding metal. Other materials are however used for both the hard phase and for binding. Carbides, carbonitrides or nitrides of titanium, niobium, vanadium, or chromium can for example be found as the hard phase. Other binding matrix materials could be nickel or iron. The

combination of the hard phase and the binder provides a desirable balance of wear resistance, hardness, and toughness. Cemented carbide inserts are usually provided with a ceramic coating, further increasing the hardness and wear resistance of the tool [1].

2.2.2.2 Ceramic

Ceramic inserts are hard, brittle and can withstand high temperatures. They are usually made of oxides or nitrides and the most common compositions are Al_2O_3 or Si_3N_4. The disadvantageous property of brittleness is improved by fiber reinforcement with SiC-whiskers. This makes the insert tough, but also resistant to thermal shocks. Ceramic inserts are manufactured with similar sintering techniques as used in cemented carbide production. Coatings, like TiN, are common on ceramic inserts and provides similar mechanical enhancements as coated cemented carbides. Ceramic inserts are not very common in industrial machining, but there are certain machining processes and workpiece materials that suits the tool material well. For example, pure oxide ceramics is a good choice for finishing operations when machining cast iron [1].

2.2.2.3 Cubic boron nitride cBN

Cubic Boron Nitride (cBN) is the second hardest known material and is not found in any form in nature. Its hardness is retained at elevated temperatures, and it is inert to iron. These properties make it an ideal material for machining abrasive ferrous materials [1]. Polycrystalline cubic boron nitride (pcBN) is a homogenous material made of cBN grains and a ceramic, metallic or wBN binder that is sintered and bound together. PcBN materials are graded from high to low, depending on what type and amount of binding material is used. PcBN can be completely binderless, and each grade have their respective application areas. Among other applications pcBN is an appropriate choice for machining of hardened steels and high-speed machining of GCI. This due to its extreme hardness, its high levels of strength and toughness, and its high level of thermal conductivity [1].

2.3 Tool wear

The load in a machining operation causes the cutting tool to continuously deteriorate until its wear criterion is reached or tool failure occurs. The tool wear criterion is the point where replacement of the tool is necessary to avoid failure. The criterion is set with regards to permitted tolerances and surface quality. Therefore, the tool wear criterion can be set differently depending on if it is a rough or fine turning operation. The wear criterion should not be confused with the tool life criterion, which is the point of failure, i.e., when the tool fails to function as intended in a given application [1].

The interaction between tool and workpiece leads to several load factors acting on the cutting edge. The main load factors are mechanical, thermal, chemical, and abrasive loads. These factors lead to a range of wear mechanisms being present in the process. The mechanisms are further explained in the subsequent section [10].

2.3.1 Tool wear mechanisms

Common tool wear mechanisms in metal cutting are abrasion wear, chemical wear, fatigue wear, and adhesion wear. The dominating mechanisms in a machining process is determined by the tool materials ability to resist the loads it is subjected to [10].

2.3.1.1 Abrasive wear

Abrasive wear is basically hard particles on the workpiece surface grinding the tool material. It is the most common tool wear mechanism, and the mechanical load on the insert results in flattening of the flank face. It is always important to have a harder tool material than workpiece material, but hard inclusions and carbides in the workpiece material can still wear the insert [10].

2.3.1.2 Chemical/Diffusion wear

When chemical or diffusion wear is present, a crater on the rake face of the insert can often be observed. That is the result of an atomic interchange, where ferrite transfers from the workpiece to the tool, and tool material transfer into the chip. This is a temperature dependent mechanism and is therefore likely to occur at higher cutting speeds. The amount of wear is often determined by the affinity of the tool material to the workpiece material [10].

2.3.1.3 Oxidation wear

Turning operations generate elevated temperatures. High temperatures and the presence of oxygen leads to oxidation of metals. Oxides of tungsten and cobalt are porous and are easily removed from the tool, resulting in wear. There are however oxides that makes the material harder, which means that some tool materials are more prone to oxidation wear than others [10].

2.3.1.4 Fatigue wear

Fatigue wear occurs during cyclic loading. It could be temperature fluctuation or variations in cutting forces. Intermittent cutting leads to cyclic heating and continuous mechanical shocks of the tool edge, so such machining is prone to fatigue wear. Plastic deformation is the most common result of fatigue wear [10].

2.3.1.4 Adhesion wear

Workpiece material can be pressure-welded onto the insert, which is called adhesion wear. This primarily occurs at lower temperatures, i.e., at low cutting speeds. This can lead to built-up edges (BUE) on the rake face, which can be ripped off by the cutting forces. This results in notches or fractures on the tool. BUEs can also interfere with the machined surface causing poor surface quality [10]. If the process temperatures are sufficiently high, an adhered layer forms while very little substitution of material takes place. This results in built-up layers (BUL) instead of BUEs. These are not as easily sheared off and can act protective on the edge. However, the layers change the geometry of the cutting edge which influence the tolerances and surface quality, without breaking the tool [1].

2.3.2 Tool wear types

The aforementioned tool wear mechanisms cause the insert to deteriorate in different ways. The following sections explain several wear types caused by these mechanisms.

2.3.2.1 Flank wear

As the name implies, flank wear occurs on the flank face of the insert, along the cutting edge. It is mainly caused by abrasive wear and leads to poor surface quality and inaccuracy due to changes in edge geometry [10]. The wear pattern is depicted in *Figure 8*. The blunted cutting edge makes the clearance angle approach zero followed by an increase in heat generation and cutting resistance [1].
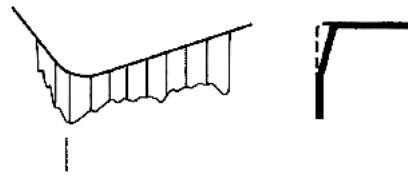

Figure 8. *Depiction of flank wear* [10].

The international standard for tool life testing of single-point turning tools states that the type of wear that is most likely to contribute to the deterioration should be chosen as tool life criterion [11]. Flank wear is usually the most prominent wear type during normal machining conditions. Therefore, it is often used as tool life criterion [12].
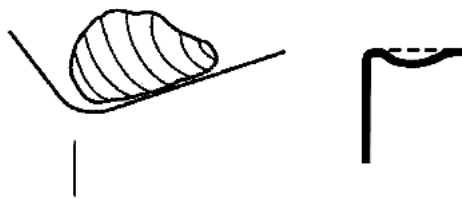
2.3.2.2 Crater wear

Figure 9. *Depiction of crater wear [10]*.

Crater wear occurs on the rake face of the insert and is mainly due to abrasive or diffusive wear mechanisms. Material is removed by hard particles in the workpiece grinding on the rake face, or by diffusive action between insert and chip caused by elevated temperatures. The geometry of the insert changes with excessive crater wear, which leads to a weakened edge and changed directions of cutting forces. This influences chip formation and chip breaking [10]. A crater wear pattern is depicted in *Figure 9*.

2.3.2.3 Plastic deformation

Increased pressure and elevated temperatures on the cutting edge causes compression of the tool and the edge run the risk of being deformed plastically. The deformed bulging edge will cause even higher temperatures, further deformations, and chip flow changes. Plastic deformation can be avoided by using a tool material with high hot hardness, and by reducing the feed and the speed of the machining process [10]. Wear due to plastic deformation is depicted in *Figure 10*.
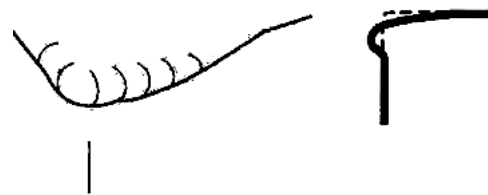

Figure 10. *Depiction of plastic deformation [10]*.

2.3.2.4 Notch wear

Figure 11. Depiction of notch wear [10].

Notch wear forms at the clearance face at the end of the cut, during the parting of the cutting edge and workpiece. It is usually due to adhesion, but elevated temperatures and exposure to the surrounding air can lead to oxidation. Notch wear influence the surface quality and weakens the cutting edge [10]. A notch wear pattern is depicted in *Figure 11*.

2.3.2.5 Thermal cracking

Cracks perpendicular to the cutting edge caused by thermal cycling, thermal load and mechanical shocks are called thermal cracks. The cracks weaken the cutting edge and will eventually cause chipping and tool failure [1]. Thermal cracks mostly occur during intermittent cutting and is therefore more common in milling than in turning. Application of cutting fluid can prevent the formation of thermal cracks [10]. A depiction of thermal cracking is found in *Figure 12*.
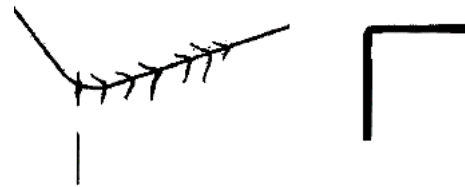

Figure 12. Depiction of thermal cracking [10].

2.3.2.6 Mechanical fatigue cracking

Figure 13. Depiction of mechanical fatigue cracking [10].

Intermittent cutting force shocks can cause cracks parallel to the cutting edge. The shock loads are not large enough to cause fracture, but the cyclic loading leads to fatigue deformation [10]. *Figure 13* shows an example of mechanical fatigue cracking.

2.3.2.7 Chipping

Loss of material along the cutting edge due to local breakage instead of continuous wear is called chipping. There are several causes to chipping, but cyclic loading like in intermittent milling is usually present [10]. Consequences of chipping are limited in rough turning, except that the risk of failure increases. In fine turning however, the surface roughness is influenced and can increase the rejection rate if the wear is not monitored properly [1]. Chipping is depicted in *Figure 14*.

Figure 14. Depiction of chipping [10].
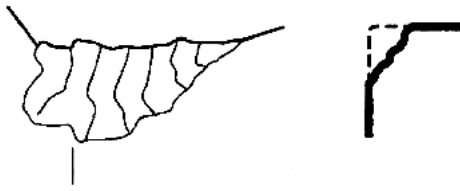
2.3.2.8 Fracture

Fracture is what occurs when the tool reaches the point of failure. Fracture due to bulk breakage are often what other wear types eventually end up in. Fracture can however arise momentarily due to for example heavy cutting data or a demanding workpiece material. A wear fracture is depicted in *Figure 15*.

Figure 15. Depiction of Fracture [10].

2.3.2.9 Built-up edge BUE

A BUE is the addition of workpiece material to the cutting edge and rake face. The added material gets pressure-welded on the insert at relatively low temperatures. This makes it a cutting speed related wear type, but other reasons behind the formation do occur. The BUE changes the geometry of the insert and increases the risk of tool material separating. Apart from the risk of rapid tool failure, BUE also heavily influences the surface texture of the workpiece [10]. A BUE is depicted in *Figure 16*.
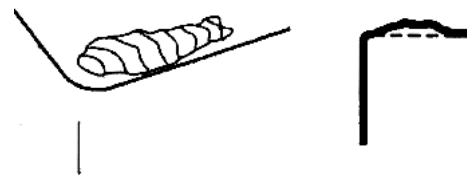

Figure 16. Depiction of BUE [10].

2.3 Grey cast iron

Cast iron is a cast alloy of predominantly iron and carbon, but other elements can be included. It is made by melting pig iron, scrap iron and other additions. The material is often alloyed with elements like silicon and manganese, but one can also find special additions like nickel, aluminum, chromium, molybdenum, tungsten, copper, vanadium, and titanium in the material [13]. What differentiates it from steel is the high carbon content of at least 2.14 wt%. Most cast iron does however contain between 3-4.5wt% carbon. Within this composition range the material melts at considerably low temperatures, between approximately 1150°C and 1300°C. This feature makes the casting procedure less cumbersome [14].

Cast irons can be divided into gray iron, ductile iron, white iron, malleable iron, and compacted graphite iron. Each kind comes with its own set of properties [14]. A majority of all industrially produced castings consists of cast iron, and the predominant type is grey iron [1].

2.3.1 Phases and microstructure

Stable iron at room temperature is called ferrite. Mechanically, free ferrite is soft and ductile. Therefore, large amounts of free ferrite are avoided in machining materials to avoid adhesive wear on the cutting tool [14].

Cementite is an iron carbide phase that is very hard and brittle. The strength of steel is enhanced by the presence of cementite, but the phase in its free form is not desired in machining applications, since the hard particles accelerate tool deterioration through abrasion [14].

Pearlite is a lamellar microstructure built up of ferrite and cementite. The mechanical properties of pearlite are intermediate between ferrite and cementite, making it suitable for machining purposes [14].
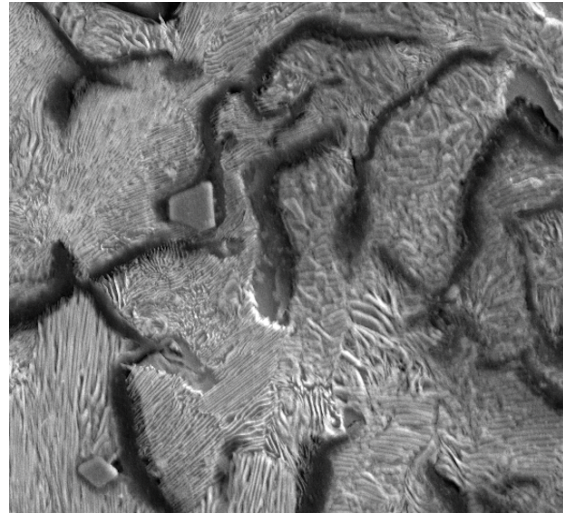

Figure 17. *Grey cast iron microstructure.*

What characterizes GCI visually are the graphite flakes that form inside the material during solidification. The microstructural matrix surrounding the flakes usually consists of pearlite. Areas of free ferrite and free cementite are also found in the microstructure [1]. A typical GCI microstructure is shown in *Figure 17*.

Studies have shown that microstructural properties get affected by production factors such as cooling rate. Schmidt (2018) showed that pearlite hardness and pearlite fineness in GCI casting was dependent on the cooling rate during pearlite transformation. This is illustrated in *Figure 18* and shows that the hardness of one kind of microstructure can vary on a batch-basis [15].
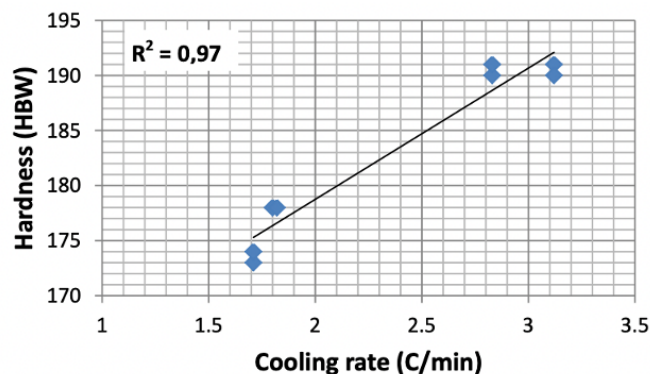

Figure 18. *Hardness Vs. Cooling rate of pearlite in GCI [15].*

Phosphorus in iron often occur as an iron-phosphide called steadite (Fe_3P). It solidifies at grain boundaries and make up a very hard and brittle phase [16]. In the right amounts steadite can increase wear resistance and fluidity but is regarded a defect once excessive amounts cluster at the boundaries. These clusters can lead to shrinkage problems and embrittlement. Steadite is a eutectic between iron and phosphorus, so it is last to solidify. Therefore, steadite can be surrounded by solid material before it has solidified completely. Shrinkage during solidification of steadite can therefore lead to microscopic voids in the structure [17].

2.3.2 Graphite

The graphite flakes in GCI have dampening and chip breaking characteristics, and they lubricate the cutting tool. Therefore, the presence of graphite flakes improves machinability. The graphite does however act as stress concentrators, which results in a brittle material that fails under tension without plastic deformation [18]. This holds especially for tensile loads, where the material shows tendencies to be weak and brittle. Under compressive loads, GCI is however much stronger and more ductile [14].
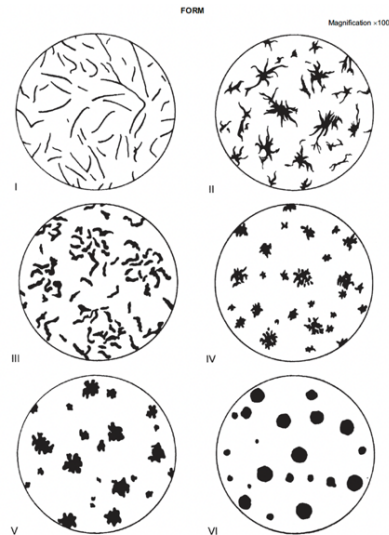

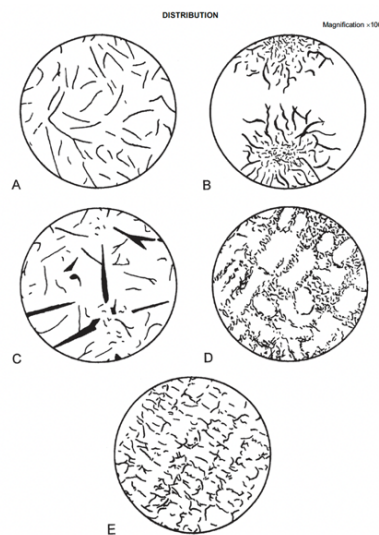*Figure 19. Principal graphite forms in cast-iron materials [19].*

Figure 20. Reference images for graphite distribution (form I) [19].

The graphite structure is affected by several factors, like carbon content, alloying elements, and cooling time. Rapid cooling leads to smaller flakes, and slow cooling enables bigger flakes to form. Because of that, bigger flakes are often found in the core of a material, while flakes near the surface tend to be smaller in size [18].

Figure 21. Reference images for graphite size (form I) [19].

ISO Standard ISO 945-1:2008 classifies the microstructure of graphite structure in GCI based on form, distribution, and size of graphite flakes. *Figure 19-Figure 21* show a selection of the classifications that has been produced for comparative visual analysis [19].

2.3.3 Inclusions

An inclusion is a chemical compound that gets trapped in a material during processing, for example when melting and pouring GCI. The inclusions present in a workpiece will influence the machinability of the material. Inclusions can be both desirable and undesirable. An example of desirable inclusions are Si-inclusions, which get soft at high temperatures, retarding tool wear at high cutting speeds. Appropriate amounts of MnS-inclusions can also be desired since they dampen and lubricate the cutting tool [10]. Presence of MnS has also shown to reduce the contact length [2]. Undesirable inclusions are aluminates, spinells, and other hard materials. These inclusions together with carbide forming elements like Ti, N,V, Cr and Nb are very hard and abrasive and leads to excessive tool wear [10].

2.3.4 Natural ageing

GCI left in room temperature experience increased strength and hardness. This process is called natural ageing and affects the materials machinability. The main part of the age strengthening occurs within the first six to ten days after casting [20]. As time proceeds, interstitially freed atoms like oxygen diffuse from the casting, which often improves machinability [1]. The process is both time and temperature dependent and can be accelerated by letting the material age at elevated temperatures [21]. However, machinability is not always improved by natural ageing. Studies have shown that GCI with just pearlite and cementite can show exacerbated machinability, while microstructures containing free ferrite show improved machinability after ageing. The fact that machinability can improve with increased hardness due to ageing can be explained by the energy requirement for chip formation. In unaged GCI, the soft ferrites absorb energy and deforms plastically resulting in BUEs. This leads to increased cutting forces and excessive tool wear. An aged GCI however, with increased hardness, allows a smoother chip breaking process with less plastic deformation and lowered cutting forces [22].

2.4 Machinability

The concept of machinability has no clear definition. It includes a range of factors like for example tool properties, material properties, and cutting data. One description of the concept is how a certain workpiece material can be machined in a way so the desired levels of size, form and surface roughness can be reached. The production cost can also be included in the description of machinability. This thesis focuses on the material factors that affect machinability, and these can generally be divided into 5 groups. These groups are represented by the materials ductility, strain hardening, thermal conductivity, hardness, and abrasiveness. To get a comprehensive overview of the machinability of a material, a polar diagram like the one exemplified in *Figure 22* can be implemented [1].
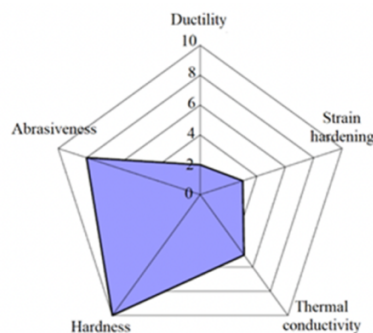

Figure 22. Example of polar machinability diagram [3].

A materials ductility indicates its ability to deform plastically without failing. The ductility value of the polar diagram is preferably low. This since it helps with for example chip breakage, and since high ductility often corresponds to increased adhesiveness of the material [1].

Strain hardening occurs in the deformation zone on the newly cut surface of the material. A further hardened surface increases the load in subsequent passages. Therefore, a high level of strain hardening is undesirable in most machining applications [1].

The friction created between the tool and the workpiece generates elevated temperatures. High heat in a cutting process can lead to thermal cracking and other temperature induced problems. The generated heat should therefore be transported from the cutting zone into the surroundings, i.e. a high value of thermal conductivity is desired [1].

The hardness of a material represents its resistance to plastic deformation. The hardness can both improve and impair the machinability. A hard material can be desired, since soft materials are prone to act adhesive on the tool edge, and hard particles can act as fracture indicators, enhancing chip breaking. On the other hand, if the hardness of the material and its inclusions approaches the hardness of the cutting tool, failure is expected. This makes the material hardness a measure of machinability only when comparing materials that are similar in composition or characteristics. Measuring the microhardness in a sufficient number of points enables statistical representation of the materials hardness. By doing that, both mean values and hardness variations can be observed [1].

A materials abrasiveness is hard to quantify, but low abrasiveness is desired. One way to decide the abrasiveness is to observe the mean microhardness value, the difference in hardness between phases, and the form and size of hard particles within the material. This method has not been validated yet but show promising results [1].

2.4.4 Chip segmentation

The chip segmentation of a machining process is strongly correlated with the behavior of the dynamic cutting forces. A tangible segmentation indicates a high variation index, a longer contact time, and big tool movements resulting in poor surface quality. The chip formation varies with machining parameters and type of workpiece material. A materials tendency to deform differs with stress changes in the shear zones and results in chip geometries represented in *Figure 23*. A segmented chip formation is mainly associated with lamellar and segmented chips, and when machining brittle materials, like GCI, segmented and discontinuous chips are most likely to occur [1].
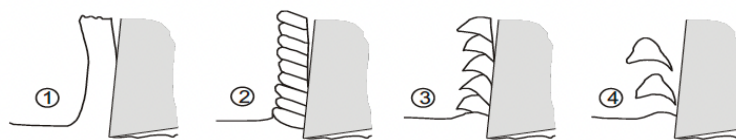
Figure 23. 1. Flow chips, 2. Lamellar chips, 3. Segmented chips, 4. Discontinuous chips [1].

In *Figure 24*, the geometry of the chip segmentation process is illustrated. This model can be used to analyze the chip segmentation sequence and the vibrations that comes with it [1].
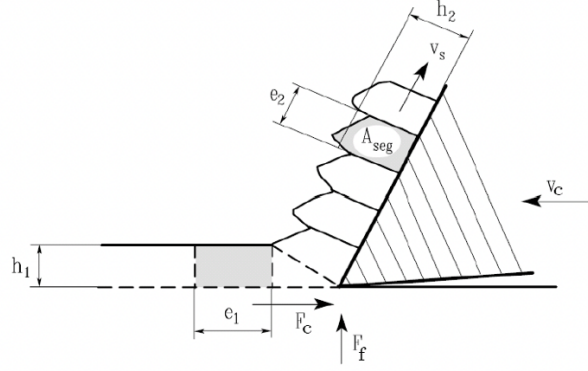
***Figure 24**. Geometry of chip segmentation process [1].*

The segmentation distance e_1 represents the distance the tool must travel into the workpiece to produce one chip segment. Due to compression in the process, the chip thickness and the segmentation distance changes, and are represented by h_2 and e_2. If widening of the chip can be neglected, the chip area can be computed. This makes it possible to calculate the segmentation distance according to ***Equation 10*** [1].

$$A_{seg} = e_1 h_1 = e_2 h_2 \Rightarrow e_1 = \frac{h_2}{h_1} e_2$$

Equation 10

Knowing the cutting velocity and the segmentation distance, one can calculate the time it takes to produce a chip. By inverting that time, one obtains the segmentation frequency, as in ***Equation 11*** [1].

$$t_s = \frac{e_1}{v_c} \Rightarrow f_s = \frac{v_c}{e_1}$$

Equation 11

The amount of chips produced during a meter of tool engagement is called the segmentation disturbance index, ρ_s, and is obtained by inverting the segmentation distance. This results in another expression for the segmentation frequency found in ***Equation 12*** [1].

$$f_s = \rho_s v_c$$

Equation 12

It is possible to determine the segmentation frequency in an experimental environment. This can be done by analyzing and measuring the chips produced during machining. With a known cutting speed, the frequency is obtained through ***Equation 13***.

$$\begin{cases} e_1 = \dfrac{h_2}{h_1} e_2 \\ f_s = \dfrac{v_c}{e_1} \end{cases} \Rightarrow f_s = \frac{h_1 v_c}{h_2 e_2}$$

Equation 13

When collecting data of dynamic cutting forces and zooming into a narrow time frame of approximately a few milliseconds, one can see the amount of chip segments produced by observing the number of peaks within that time frame. That time frame, divided by the number of segments produced, results in the segmentation frequency. A more precise way to obtain the segmentation frequency is to present the cutting forces in the frequency domain using Fourier transform analysis. By doing so, one can see a characteristic frequency, corresponding to the segmentation frequency [1].

2.5 Nanoindentation

Nanoindentation is a technique for measuring mechanical properties at small scales. An indenter tip, conventionally made of diamond, is applied with a mechanical load to a sample material. The force and displacement of the tip are recorded at both loading and unloading of the indenter. A typical load-displacement curve from nanoindentation is depicted in *Figure 25*. The most common units measured by nanoindentation are elastic modulus and hardness. When measuring hardness, the maximum force is divided by the indentation area to obtain the Berkovich hardness value in Pascal units. The indentation area can either be measured with in-situ technology or with microscopy [23].
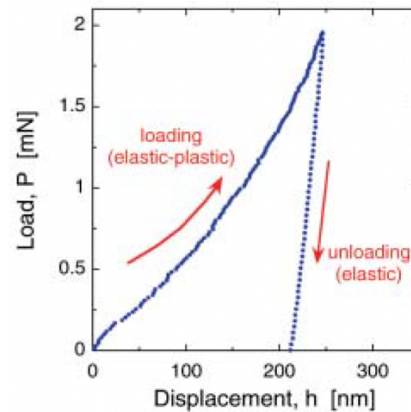
Figure 25. Load-displacement curve from nanoindentation [23].

2.6 SEM/XEDS

Scanning electron microscopy (SEM) is a useful investigative tool for observing microstructural features. The principle of the microscope is that it scans the surface of a sample with a focused electron beam. Reflected or backscattered electrons are collected, and visual information can be gathered based on the gray-scale intensity between the present phases. The number of backscattered electrons corresponds to the atomic number, and particles with a high atom number will generate a brighter image than particles with a low atomic number.

Analysis of the elemental composition in a sample can be done by energy-dispersive X-ray spectroscopy (XEDS) using the characteristic X-ray spectrum of the material sample [24]. An example of elemental mapping of a material using SEM/XEDS is shown in *Figure 26*, where inclusions of TiC and MnS are found in the sample.
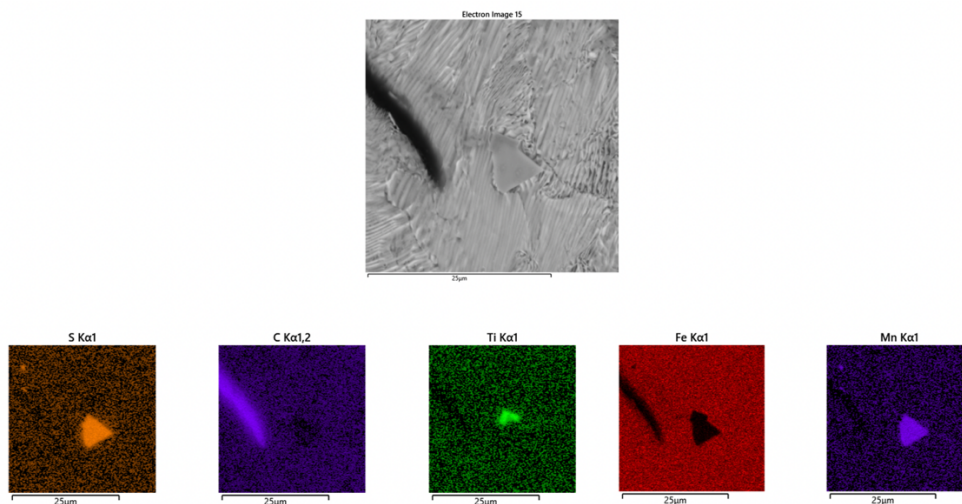

Figure 26. Example of element mapping with XEDS.

2.7 Statistical analysis

Experimental data can be analyzed by comparison with statistical distributions. For a continuous distribution, a probability density function and a cumulative distribution function can be generated in search of correlation or causality between data. One distribution often found in the context of production is the Weibull distribution. The cumulative Weibull distribution function can be found in *Equation 14*. If the constants α and β can be determined, an expression representing the experimental data can be obtained [25].

$$F_{single\ dist.} = \left(1 - e^{-\left(\frac{x}{\beta}\right)^{\alpha}}\right)$$

Equation 14

Since several factors often influence the results of production and experiments, several distributions can be needed to describe the data. The cumulative distribution functions for double and triple Weibull distributions are found in *Equation 15* and *Equation 16*. If all the constants can be determined, where ψ_n provides the influence from each distribution, a reliable model of the data is obtained [25].

$$\begin{cases} F_{double\ dist.} = \psi_1 \left(1 - e^{-\left(\frac{x}{\beta_1}\right)^{\alpha_1}}\right) + \psi_2 \left(1 - e^{-\left(\frac{x}{\beta_2}\right)^{\alpha_2}}\right) \\ \psi_1 + \psi_2 = 1 \end{cases}$$

Equation 15

$$\begin{cases} F_{triple\ dist.} = \psi_1 \left(1 - e^{-\left(\frac{x}{\beta_1}\right)^{\alpha_1}}\right) + \psi_2 \left(1 - e^{-\left(\frac{x}{\beta_2}\right)^{\alpha_2}}\right) + \psi_3 \left(1 - e^{-\left(\frac{x}{\beta_3}\right)^{\alpha_3}}\right) \\ \psi_1 + \psi_2 + \psi_3 = 1 \end{cases}$$

Equation 16

The accuracy of the statistical model can be determined by calculating its error using *Equation 17* below. *ERR* is expressed in error percentage, S_j is the empirical distribution function, and j is the amount of datapoints [25].

$$ERR = \frac{100}{j} \sum \left| \frac{S_j - F(x_j)}{S_j} \right|$$

Equation 17

2.8 Cutting data optimization

In Hägglund's doctoral thesis *Methods and Models for Cutting Data Optimization* (2013), the author divides the process of optimizing cutting data into optimization for new or already existing parts. This thesis focuses on existing parts, and the procedure suggested by Hägglund can be found in *Figure 27* [26].
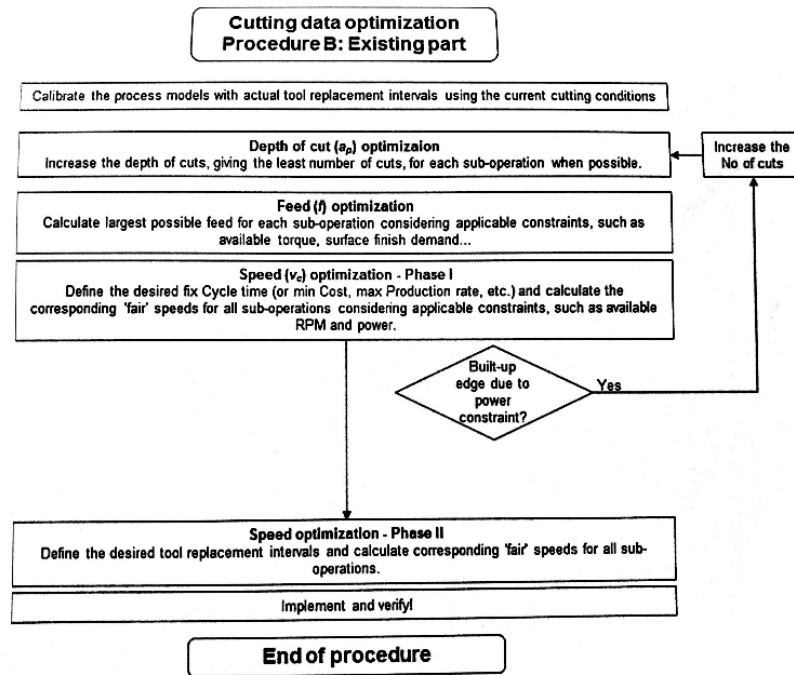
Figure 27. Cutting data optimization procedure for existing part [26].

Hägglund emphasizes the importance of first establishing an optimal depth of cut, then the feed rate, and lastly the cutting speed. This since the process time and cost are more affected by the cutting depth and the feed, than by the velocity. Therefore, the cutting speed should be an adaptation to the chosen values for depth and feed [26].

The most effective way to reduce cycle time without affecting the tool cost negatively is by reducing the number of cuts, i.e., to maximize the cutting depth. In addition, a_p is the parameter that affects tool wear the least. Power constraints and insert geometry influences the choice of cutting depth, and **Equation 18** shows that the depth can be maximized by adjusting the major cutting angle and choosing an insert with a long cutting edge [26].

$$a_{p,max} = b_{max} sin\,(\kappa)$$ ***Equation 18***

Next, one should maximize the feed. Not only because a high feed is more effective for process time and process cost than a high cutting speed, but because of the elevated temperatures. Higher feeds and speeds both cause increased temperatures, but a temperature caused by a high feed rate tend to occur in the sheared chips. Elevated temperatures due to high speed tend to stay on the cutting edge, obstructing machinability. There are however physical constraints to maximizing feed. Several parameters influence the surface quality of a workpiece, but the theoretical surface roughness can be explained by **Equation 19** below [26].

$$R_a = \frac{f^2}{8r}$$ ***Equation 19***

The equation shows that an increased feed is a compromise with surface quality. This can be compensated for partially by choosing an insert with a more robust geometry, i.e., with a larger nose radius.

A constraint for maximum feed can be found in *Equation 20* below.

$$f_{max} \leq 2\sqrt{a_p(2r - a_p)}$$ *Equation 20*

This does not hold for so called wiper inserts, which has a geometry made for higher feeds. With a wiper inserts one can double the feed for maintained surface quality or double the surface quality without changing the feed.

When optimizing the cutting speed, one must consider the rpm and the power constraints. These are expressed in *Equation 21* and *Equation 22* [26].

$$v_{c,RPMmax} = \frac{\pi \cdot D \cdot RPM_{max}}{1000}$$ *Equation 21*

$$v_{c,Pcmax} = \frac{P_{c,max} \cdot 60 \cdot 10^3}{F_c}\eta$$ *Equation 22*

These optimizations above mainly focus on the process time and process costs and does not consider tool wear. When tool wear is considered, the main focus is often the cutting speed. Tool manufacturers do make cutting data recommendations based on material groups. The problem with these recommendations is that they are based on a somewhat wide range of materials, and the machinability can vary substantially between the materials in these groups. The machinability can even vary from batch to batch for the same material, depending on factors like for example ageing [26]. This is verified in a study conducted at LTH. Several factors of GCI machinability were investigated and the data in *Figure 28* was obtained. The figure suggests a positive influence of increased cutting speed up to a certain limit. Thereafter, wear drastically increases with the cutting speed due to elevated temperatures on the cutting edge. This holds for both aged and unaged materials, although the wear is less excessive for aged materials [27].
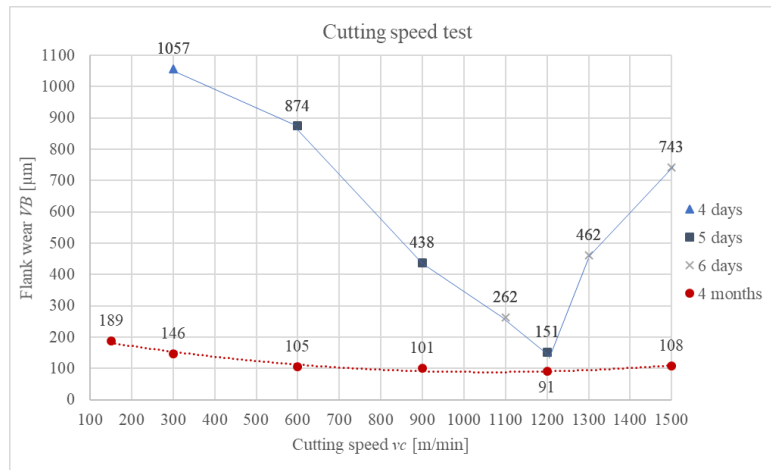

Figure 28*. Flank wear at selected cutting speeds for limited and complete ageing [27].*

One approach to find the optimum cutting speed, among other machining parameters, is to implement so called incremental production development. It is a method where one systematically alters one parameter at a time until the part cost has stabilized, before another parameter value is changed. Costs and process quality are carefully documented throughout the process. Then the outcome of part costs can be expressed as a function of the material removal rate. This gives the possibility to determine which outcome is most suitable for one's company. An example of a possible outcome for such a process can be found in *Figure 29* [25].
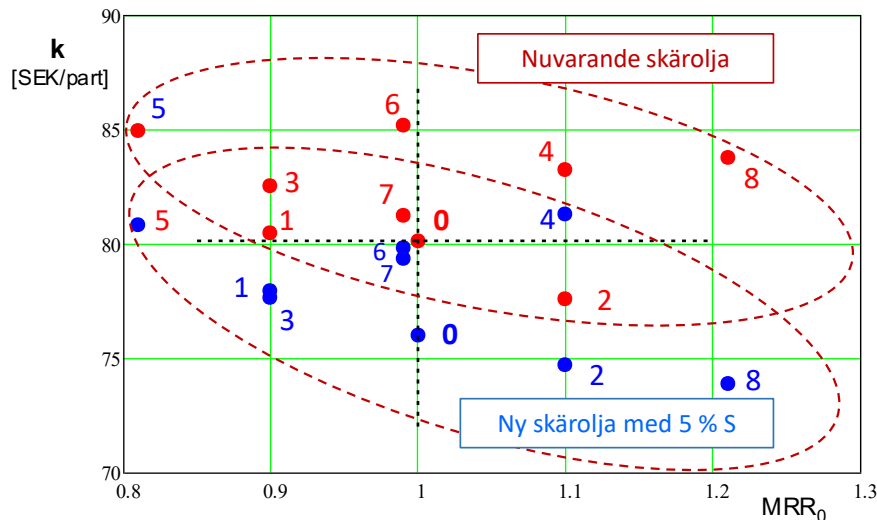
Figure 29. Part cost in SEK/part Vs. MRR for machining with two different lubricants [25].

3 Methodology

The methodology of this project was divided into three parts. The first part was partially conducted at ACF's facilities in Floby, where worn inserts were collected from the production line. These were later analyzed at LTH to answer objective question one.

The second part was conducted at the Department for Production and Materials Engineering at LTH. Experiments and analyses were done to link hardness and structural variations to machinability, i.e to answer objective question two.

To answer objective question three, previous work on optimization of machining parameters was observed in a literature survey. The survey included comparison of cutting data from ACF with the tool manufacturers recommendations. Observations from said survey were later correlated to the experimental results of this study, to find suggestions for cutting data optimization paths.

3.1 Part one – Identification of wear types and mechanisms

At ACF, the brake discs were machined on a Motch 125-VNC vertical lathe on production line 5. The discs passed five machining stations. First three rough turning stations, then a drilling operation, and lastly a fine turning station. After the fine turning, the discs were checked for tolerances. This was followed by balancing and painting of the discs before they were packed for shipment.

3.1.1 Workpiece material

The workpiece material in the production line was a Type 33 VIG130/160 brake disc. It was casted by Eurac Poole in Dorset UK. VIG130/160 is a material designation made by Volvo. The designation indicates that it is a GCI with a minimal tensile strength of 130 N/mm^2 and a hardness within the range of 160-220 HBW. The material matrix should consist of pearlite and max 5 % free ferrite. Free cementite should not exceed 2 %. Ranges for chemical composition can be found in *Table 1*. The graphite structure should have form I, distribution A and size 4 [28].

Table 1. *Chemical composition of VIG130/160 [28].*

Material designation	C %	Si %	Mn %	P %	S %	Cu %	Cr %	Ni %	Mo %	V %	Sn %	B %
VIG130/160	3.60-3.90	1.80-2.20	0.50-0.80	max 0.10	max 0.10	0.60-1.00	0.20-0.40	-	max 0.10	-	-	-

3.1.2 Machining parameters

The rough turning of the friction surfaces was divided into two passages, called OP20 and OP30. The fine turning operation was called OP50. Cutting data for each passage can be found in **Table 2**.

Table 2. *Cutting data for OP20, OP30, and OP50.*

Cutting data	OP20	OP30	OP50
a_p (mm)	1.7	0.4	0.4
f (mm/rev)	0.95	0.9	0.72-0.76
v_c (m/min)	900	800	1000

3.1.3 Cutting tools

Cutting tools were collected at predefined intervals. Every rough turning edge was considered to be worn out after 400 discs. The corresponding amount for the fine turning edges was 80 discs. Each insert had four cutting edges, i.e., the rough and fine turning inserts were replaced after 1600 and 320 discs respectively. For rough turning, CeramTec CBN insert CNGX 120416 grade WBN115 was used. For fine turning, CeramTec silicon nitride insert SCGN 090408 T grade SL500 was used. 11 fine turning insert were collected, i.e., 44 cutting edges. From the rough turning operations 10 inserts were collected. Four from OP20 and six from OP30, corresponding to 16 and 22 cutting edges respectively.

3.1.4 Analysis

All inserts were observed under an Olympus SZX7 optical microscope. First all wear mechanisms and present wear types were determined for every cutting edge. Then, in the cases with measurable flank wear, an average value was calculated. One insert from each operation was observed in a SEM microscope and XEDS analyses of the cutting edges were performed.

3.2 Part two – Process behavior

Two Type 33 VIG130/160 brake discs were provided by ACF for the second part of the study. The discs were collected from different batches with known machinability. One of the discs had reasonably good machinability, while the other one had poor machinability. These discs are hereafter referred to as GM and BM, which are abbreviations for good and bad machinability. The chemical compositions of the discs, determined at Volvo Group Truck Operations Casting Laboratory in Skövde, can be found in **Table 3** and **Table 4** below.

Table 3. *Chemical composition for disc with BM.*

Material designation	C %	Si %	Mn %	P %	S %	Cu %	Cr %	Ni %	Mo %	V %	Sn %	Ti %
VIG130/160	3.67	1.87	0.69	0.05	0.06	0.19	0.11	0.04	0.01	0.007	0.010	0.011

Table 4. *Chemical composition for GM.*

Material designation	C %	Si %	Mn %	P %	S %	Cu %	Cr %	Ni %	Mo %	V %	Sn %	Ti %
VIG130/160	3.67	1.79	0.60	0.05	0.06	0.16	0.11	0.06	0.03	0.006	0.020	0.010

The discs were machined at LTH on a Boehringer Göppingen VDF with the cutting force sensor found in *Figure 30*. An uncoated DNMA cemented carbide insert without chip breaker geometry was used, one edge for each disc. Four passages on the outside friction surface of each disc were machined with the cutting data in *Table 5*. Since the turning of the friction plane was radial, a slight decrease in cutting speed occurred during the operation. This was neglected in the calculations. The first passage was a facing operation to get a plane surface and to avoid intermittent cutting. Data from the remaining passages were used for analyses. The lathe used in the machining tests is depicted in *Figure 31*.
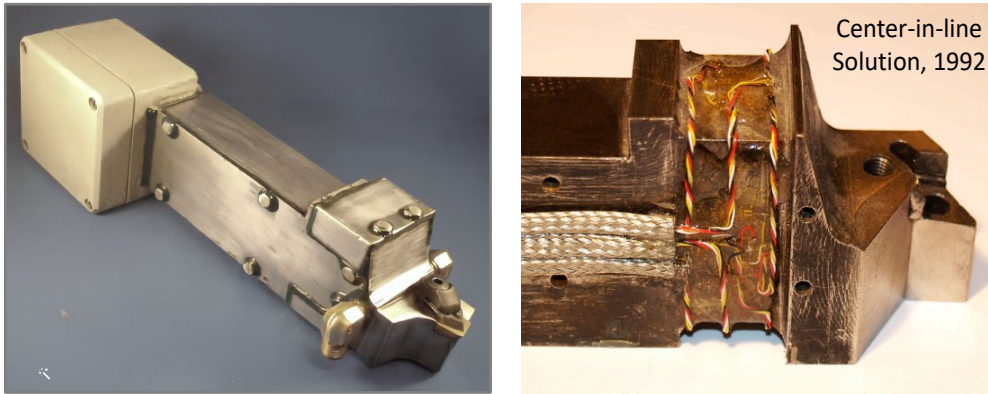
Figure 30 *Cutting force sensor with a bandwidth of 7.5 kHz in T-direction, 5.5 kHz in A-direction, and 12.5 kHz in R-direction [1].*

Table 5. *Cutting data from machining tests.*

Passage	a_p (mm)	v_c (m/min)	f (mm/rev)
1	1.5	150	0.4
2	2.5	150	0.4
3	2.5	150	0.4
4	2.5	150	0.4

Data of process behavior in terms of dynamic cutting forces were collected as a function of time with a sampling frequency of 100kHz. This data was later presented in the frequency domain using Fourier transform.

Figure 31*. Boeringer Göppingen VDF lathe used in the machining tests.*

Chips were collected from each passage for optical microscopy analysis. The average compressed chip thickness and compressed segmentation distance were measured to calculate the segmentation distance according to ***Equation 10***. The chips were also observed in a SEM microscope.

3.2.2 Sample preparation

After machining, the brake discs were cut into 10 mm x 10 mm samples and mounted in resin. Two segmented chips from each passage were prepared the same way. Each sample was then polished in intervals down to a grit of 1 μm for a mirrorlike finish. The as-polished samples were investigated for segmentation distance, hardness, and graphite structure. The samples from each disc were then etched in a 5% nitric acid ethanol solution for microstructure analysis in the SEM.

3.2.3 Nanoindentation

Hardness measurements were conducted in a nano indenter, where a Berkovich indenter tip was used to make 400 indentations in a 20x20 grid pattern. The load for each indentation was 50 mN, and the total area of indentation was approximately 1 mm^2 for each sample. ***Figure 32*** below depicts the nano indenter.
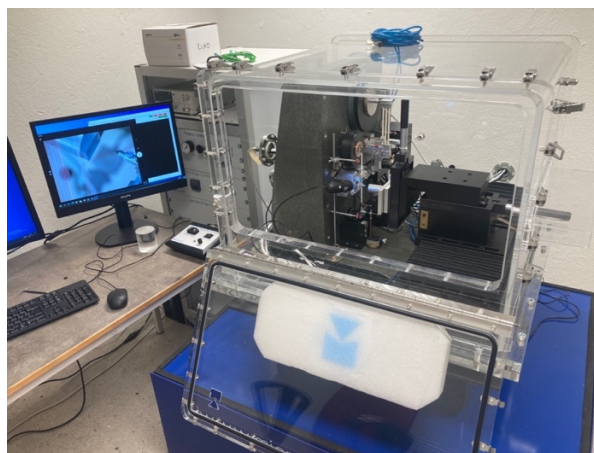
Figure 32*. Nano indenter used for hardness measurements.*

Three samples were collected from each brake disc, and the hardness was measured in radial, axial and tangential directions in the bulk of each material. Sample location and clarification of the measured directions are found in **Figure 33**. Hereafter, the directional samples will be abbreviated B_1, B_2, and B_3 for the disc with bad machinability, and G_1, G_2, and G_3 for the disc with good machinability.
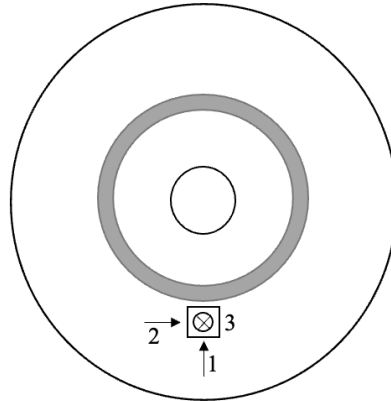
Figure 33. Sample location and measured directions. Directions: 1=radial, 2=tangential, 3=axial.

The areas around the indents were observed in an Alicona InfiniteFocus, which is an optical microscope for measurements in the μm and sub-μm range. This was done to connect hardness values to microstructure. The used microscope is depicted in **Figure 34**.
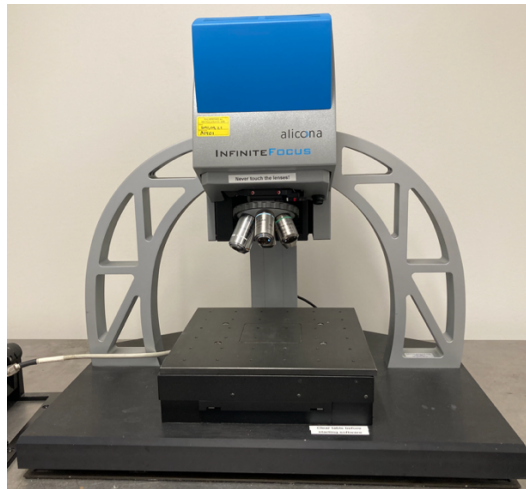
Figure 34. Alicona InfiniteFocus.

3.2.4 SEM/XEDS

Samples of both materials (direction 2) were studied in an unetched state to observe the graphite structures and for XEDS-analysis of inclusions. The samples were then etched to observe the pearlitic microstructure. Grain sizes were measured using the linear intercept method in the software *ImageJ*. Lines of known length were drawn over micrographs, which were divided by the number of intersecting grains, to get an average grain diameter.

3.2.5 Statistical analysis – Multimodal distribution

Each mode in a multimodal distribution represents different things depending on the object of study. When micro-hardness is observed, a distribution like the one in **Figure 35** can be

obtained. Here, super positioning distributions 1-3 results in the mixed distribution. Distribution 1 represents the free ferrite, ferrite inside of pearlite, and other soft particles that the indenter tip might encounter. If the indenter tip encounters a hard phase like pearlite and soft graphite at the same time, a low hardness value belonging to distribution 1 is obtained. Distribution 2 represents the pearlite in the material matrix. The third distribution represents the hardest particles encountered. It could be fine pearlite, free cementite or other carbides in the form of inclusions. The weight parameters ψ_n in *Equation 16* are weight fractions of each distribution and could, in some cases, be used to quantify microstructures in a material.
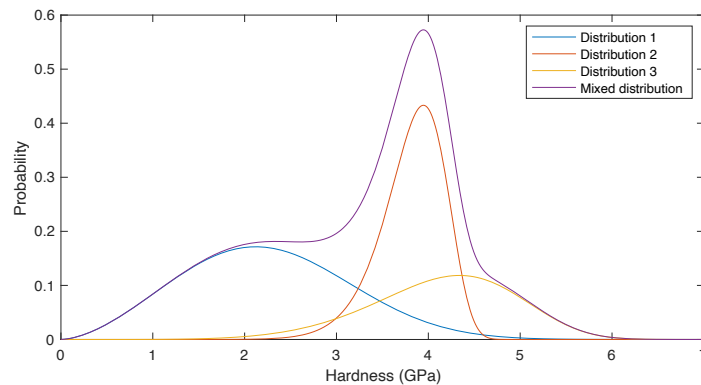
Figure 35. Example of mixed distribution.

4 Results

The following sections presents all the results obtained during the experiments and analyses. These results are later analyzed in the discussion section of the report.

4.1 Tool wear analysis

Four inserts were collected from OP20, providing 16 edges for analysis. The corresponding numbers for OP30 were six and 22, and 11 and 42 for OP50. Two edges each on inserts from OP30 and OP50 had not been used.

4.1.1 OP20

Under the microscope, edges from OP20 showed workpiece material being adhered to the cutting edge and some flank wear. The average flank wear on the investigated edges was 221.97μm. A representative image of the tool from OP20 can be found in *Figure 36*.
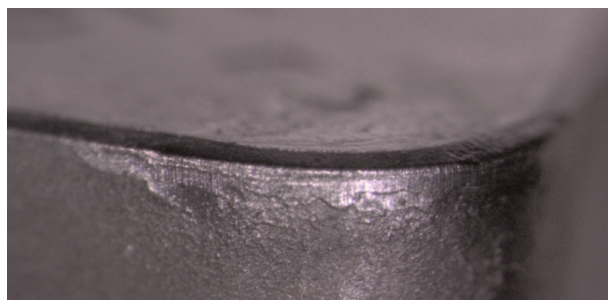
Figure 36. Representative image of tool wear from OP20.

Figure 37 show a SEM image from OP20 where workpiece material is adhered to the cutting edge. The adhesion is confirmed by a zoomed in XEDS-analysis in *Figure 38*.
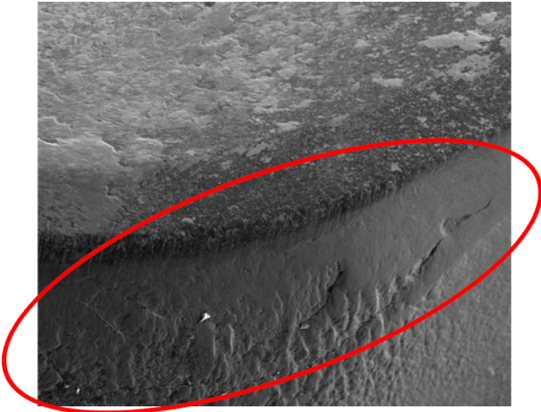
Figure 37. SEM image of cutting edge from OP20. Adhered material is found inside red ellipse.
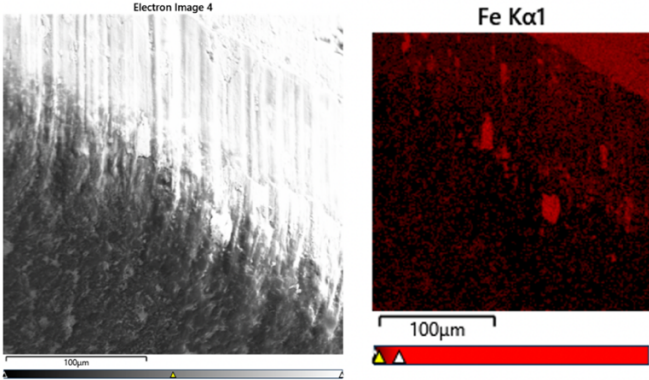
Figure 38. XEDS from inside red ellipse in Figure 37, showing adhered workpiece material.

4.1.2 OP30

Analyses of edges from OP30 showed a more aggressive wear pattern, as can be seen in *Figure 39*. An average flank wear of $308.07 \mu m$ was observed, and all inserts showed excessive crater wear. Adhered workpiece material was observed on both the flank and the rake faces.
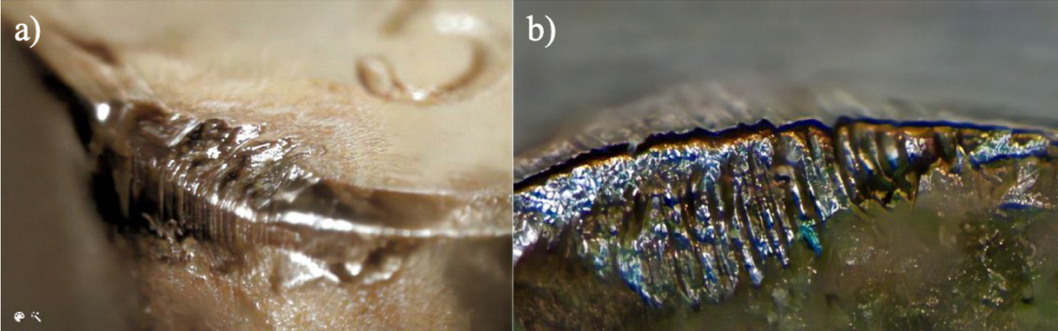
Figure 39. Representative image of tool wear from OP30. a) overview, b) crater wear on rake face.

The adhesion was confirmed by XEDS-analysis shown in *Figure 40* and *Figure 41*.
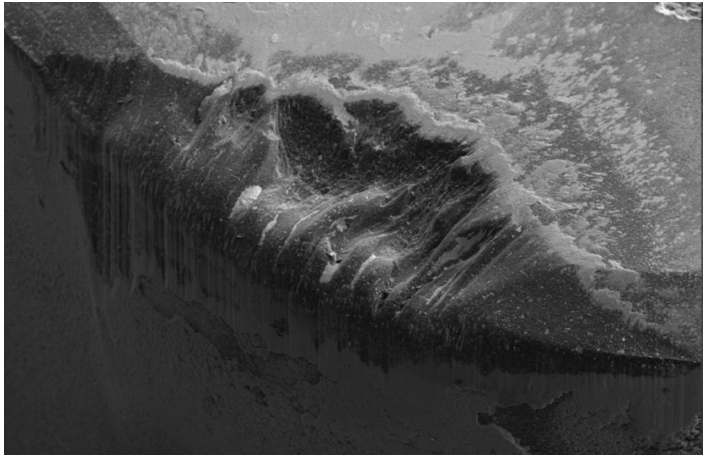
Figure 40. *SEM image of cutting edge from OP30.*
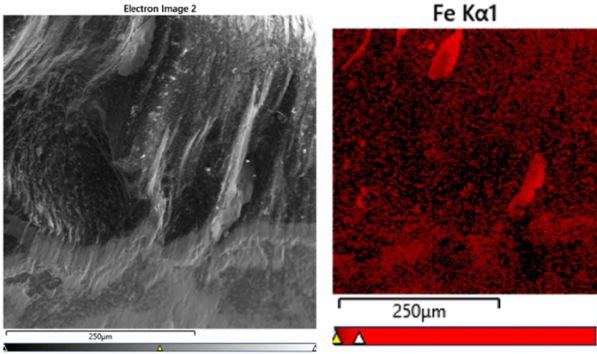
Figure 41. *XEDS inside crater of insert from OP30, showing adhered workpiece material.*

4.1.3 OP50

All inserts from OP50 had adhered layers of workpiece material on both the rake faces and the flank faces. Because of the amount of adhered material, it was not possible to measure any flank wear. A representative image of a tool from OP50 can be found in *Figure 42*.
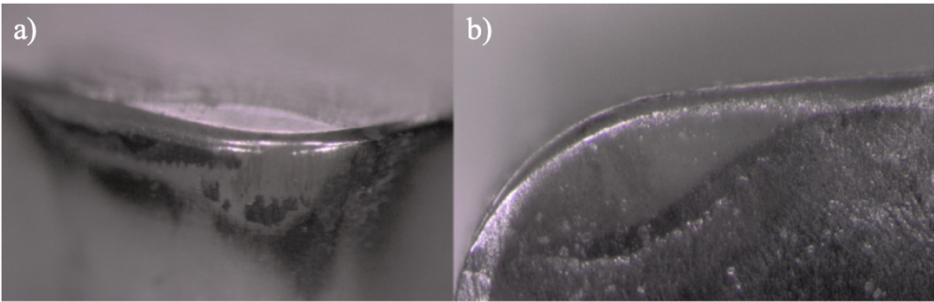
Figure 42. *Representative image of tool wear from OP50. a) overview, b) rake face.*

The adhesion was confirmed by XEDS-analysis shown in *Figure 43* and *Figure 44*.
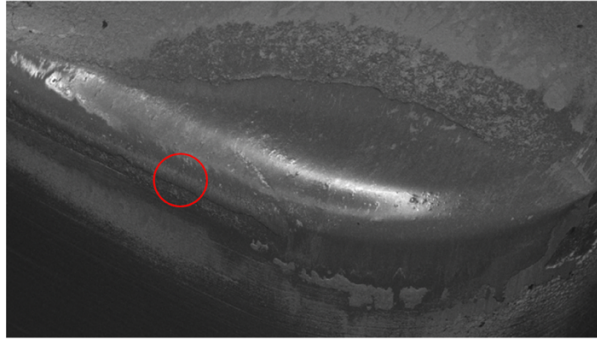
Figure 43. *SEM image of cutting edge from OP50. Red circle indicates position for XEDS analysis.*
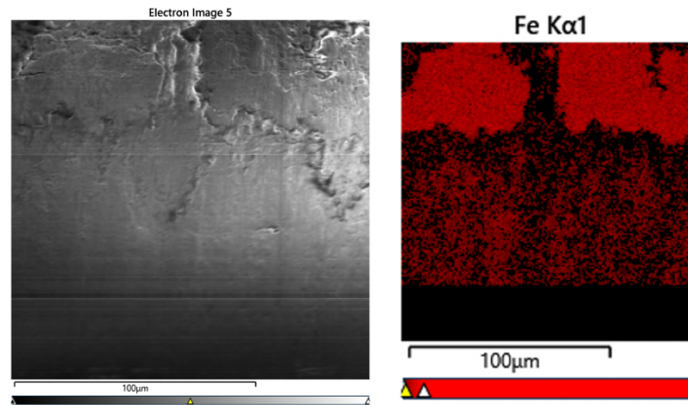
Figure 44. *XEDS of insert from OP50 showing adhered workpiece material.*

4.2 Cutting force analysis

Dynamic cutting forces were recorded during machining, and an example of how the forces look when plotted against time can be found in ***Figure 45***.
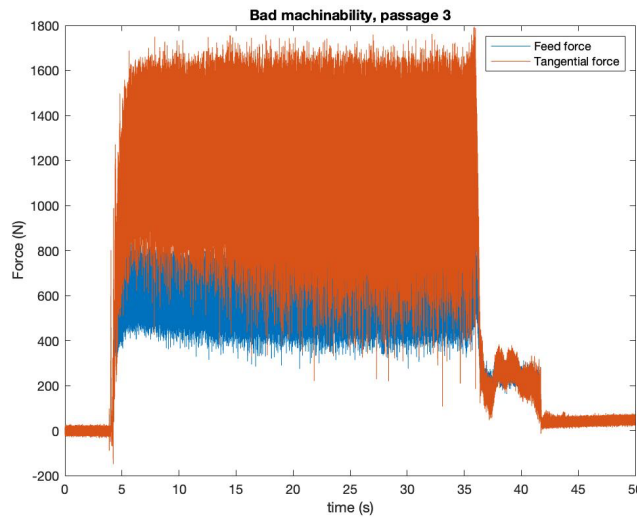
Figure 45. *Cutting forces Vs. time for third passage on BM.*

Each force component from every passage were stacked together in an array. Statistical analyses resulted in a double Weibull distribution for both materials, and the obtained mean values for the force components are presented in ***Table 6***.

Table 6. Mean forces for both materials.

	BM	GM
Tangential force (N)	1329.10	1322.80
Feed force (N)	631.72	614.25

When zooming into an arbitrary 2 millisecond timespan within steady state of the force plots, ***Figure 46*** is obtained. Here, every peak and valley correspond to a chip segment being produced. An approximation of the segmentation frequency can therefore be made to just below 2 kHz. Corresponding plots for remaining passages can be found in ***Appendix 1***.
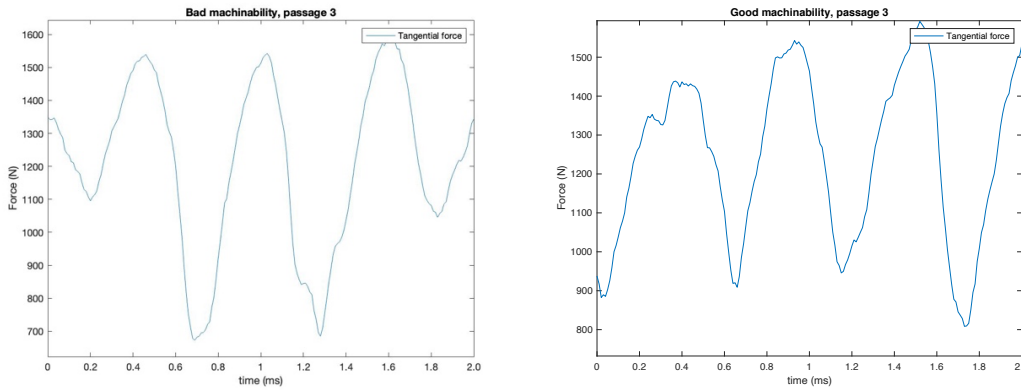
Figure 46. Main cutting forces as a function time, zoomed in to a 2ms timeframe for both materials.

If a second peak occur before load relieving, the tool is in contact with several chip segments at one time, and a force response curve as in ***Figure 47*** is obtained. This indicates problems with continuous segmentation and machinability.
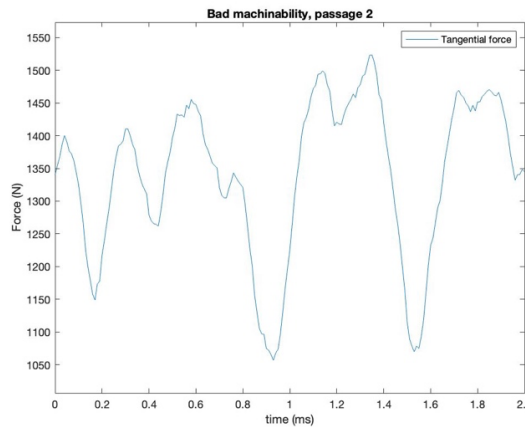
Figure 47. Example of a cutting tool in contact with several chips.

4.2.1 Load functions φ_{AT}

To understand the load distribution on the cutting tool, statistical analyses of the load functions were performed. The load functions could be described by two Weibull distributions each and model errors were 0.29 % for BM and 0.50 % for GM. Cumulative distribution functions (CDF), probability density functions (PDF), and every contributing distribution can be found

in *Figure 48* and *Figure 49*. *Figure 50* shows a comparison between the two materials, where φ_{AT} for BM is higher most of the time.
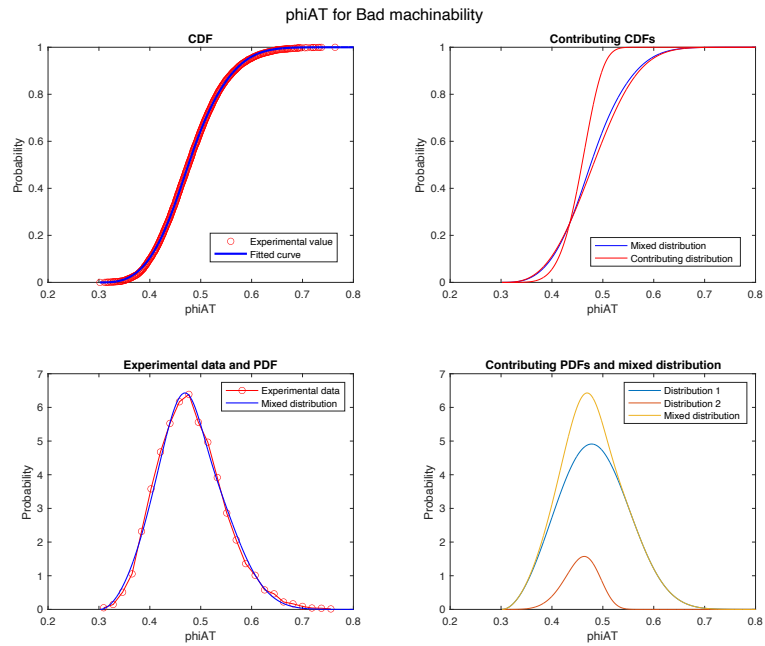

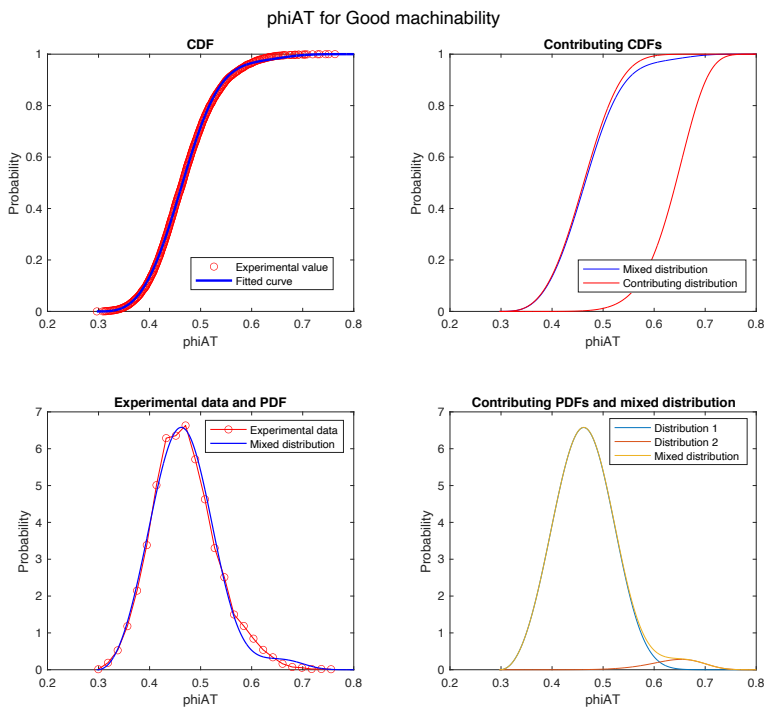***Figure 48**. Statistical analysis of load function φ_{AT} for BM.*

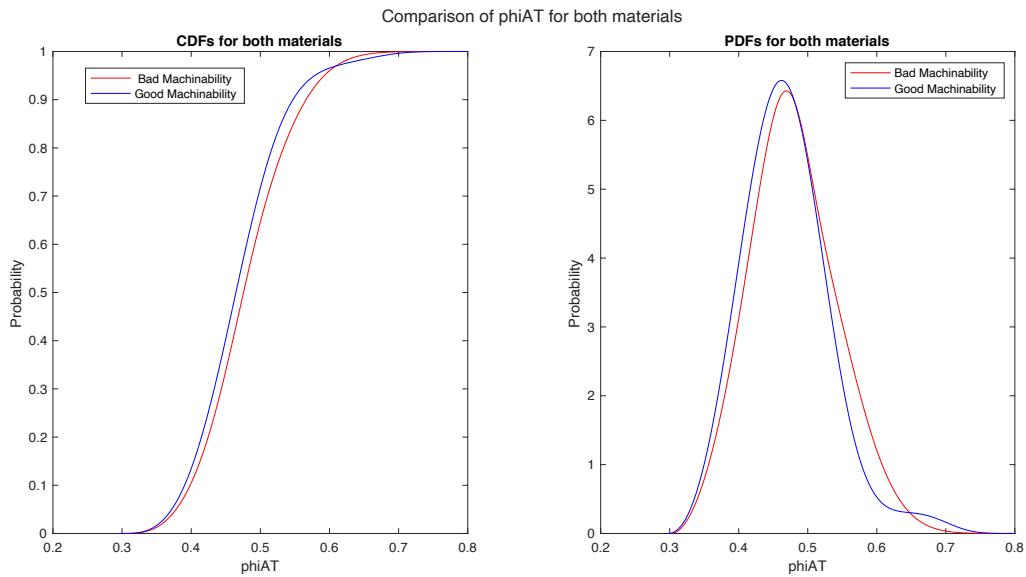***Figure 49**. Statistical analysis of load function φ_{AT} for GM.*

Figure 50. Comparison of φAT for both materials.

Plotting the load functions, zoomed into an arbitrary timeframe of 5 milliseconds, **Figure 51** is obtained. Plots of the remaining passages can be found in **Appendix 3**. Mean values for the load functions can be found both in **Figure 51** and **Table 7**.
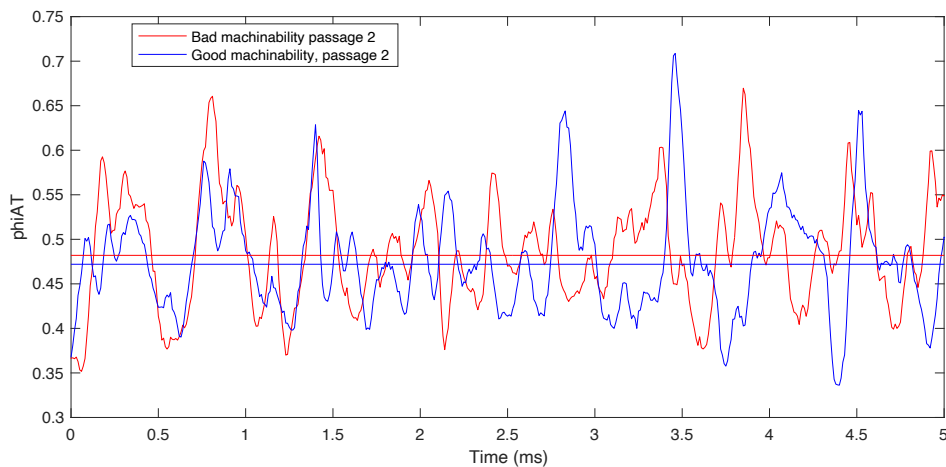

Figure 51. Load function during 5 milliseconds for both materials.

Constant value line's represent each materials mean load function.

The mean values of the load functions together with the mean values of the forces from **Table 6** show a higher φ_{AT} for BM, caused by higher feed forces.

Table 7. Mean values of load functions.

	BM Passage 2	BM Passage 3	BM Passage 4	BM Total	GM Passage 2	GM Passage 3	GM Passage 4	GM. Total
Mean φ_{AT}	0.48	0.48	0.47	0.48	0.47	0.47	0.46	0.47

Figure 52 below shows a plot of feed forces against tangential forces. Here, BM has the highest values for both the feed force (832.4 N compared to 813.2 N for GM) and the tangential force

(1713.3 N compared to 1693.8 N). It also has the lowest tangential force (645.0 N compared to 785.8 N) and is not far from having the lowest feed force (415.5 N compared to 409.1 N for GM). This indicates a high variation index and shows that the range that BM forces are distributed within is wider than for GM, while keeping a high mean value. This is confirmed by the histogram of the force data presented in **Figure 53**, and indicates a less stable process when machining BM.
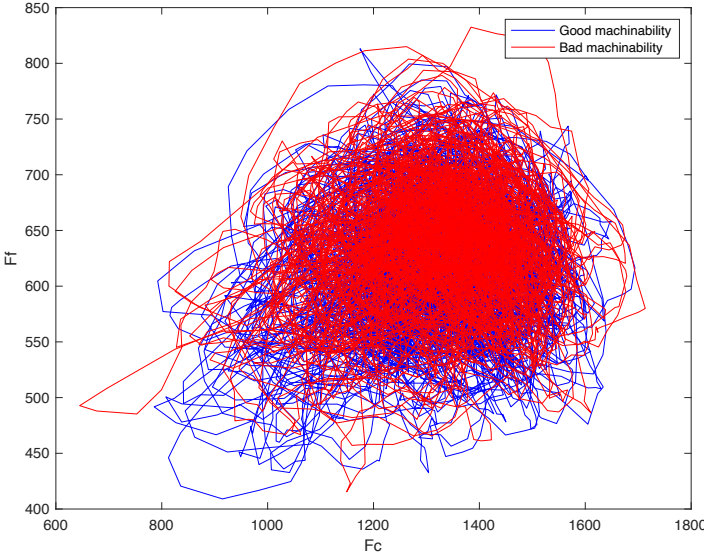

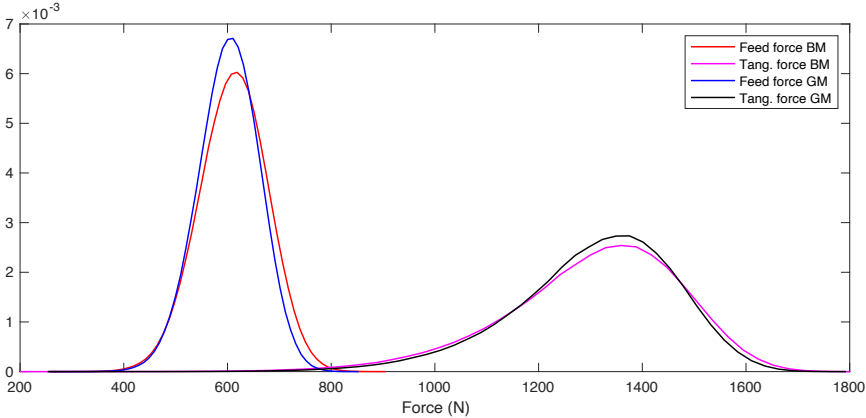***Figure 52****. Load picture, F_f Vs. F_c for both materials*

Figure 53*. Histograms of forces.*

4.3 Frequency analysis

To analyze the segmentation frequencies, Fourier transform was performed on the observed cutting forces. The segmentation distances were determined by measuring chips from the turning operations.

4.3.1 Cutting forces in the frequency domain

When transforming **Figure 46** to the frequency domain, **Figure 54** was obtained. Here, one can clearly see a characteristic frequency at 1850 Hz.
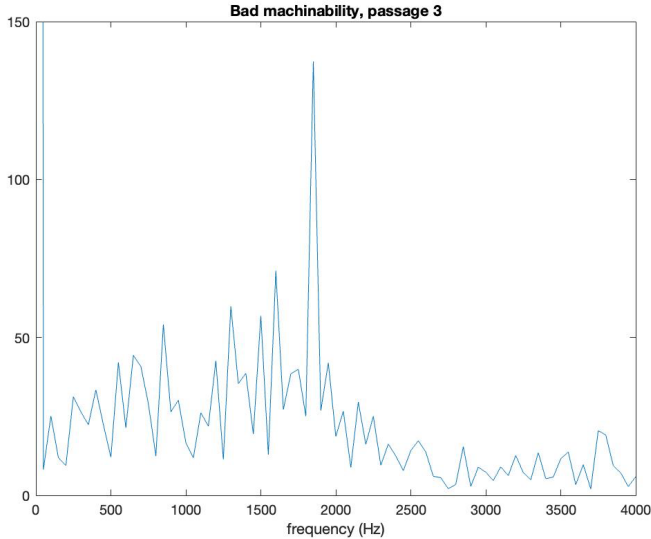

Figure 54. *Relative amplitude of frequencies for third passage on disc with BM.*

When plotting the tangential forces in the frequency domain for all passages within the same time frame, **Figure 55** is obtained. Here one can see a distribution of segmentation frequencies for each material.
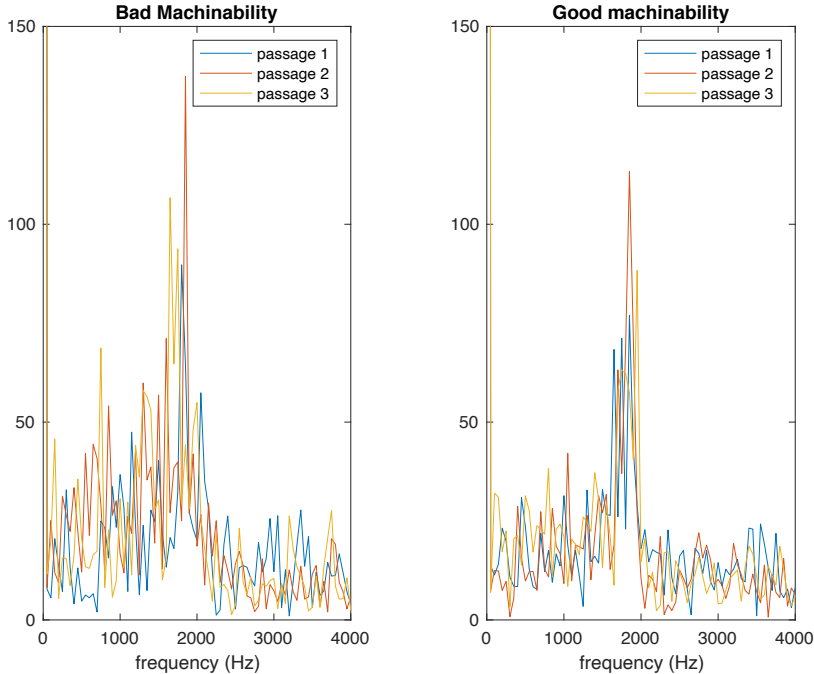

Figure 55. *Frequency plots from all passages added for each material (Bad and Good).*

Figure 56-Figure 58 shows consistently higher segmentation frequencies for GM at every passage. These are however just samples of two milliseconds. To get a more accurate picture of the segmentation for each material, other measures are necessary.
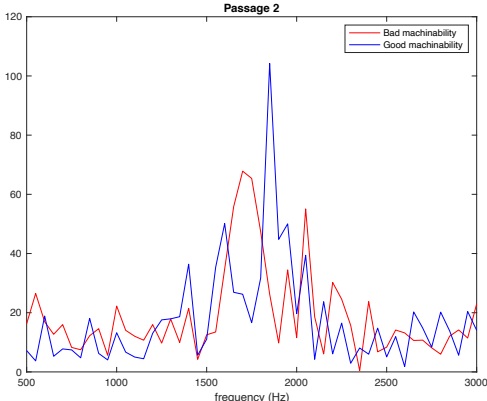

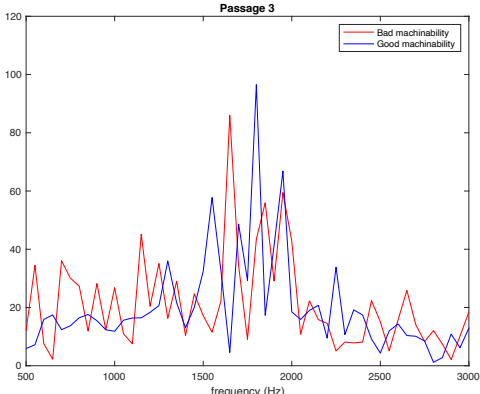**Figure 56**. *Segmentation frequencies for passage 2.*   **Figure 57**. *Segmentation frequencies for passage 3.*
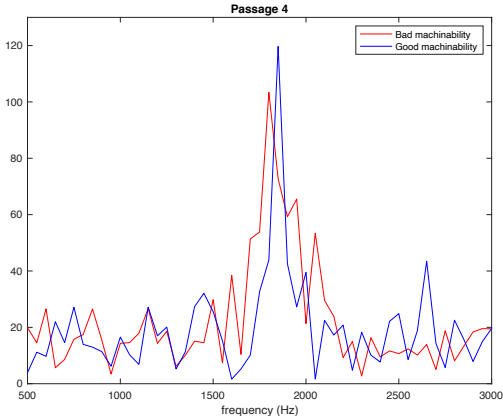

Figure 58. *Segmentation frequencies for passage 4.*

To get a mean value of the segmentation frequency for each material, an iterative program was composed. The program made iterations of two milliseconds over a 20 second timespan, recording the segmentation frequency in every iteration. This resulted in 10000 values for each passage, i.e 30000 values per material. The results can be found in *Table 8* below.

Table 8. Mean segmentation frequencies for both materials.

	Passage 2	*Passage 3*	*Passage 4*	*Total mean frequency*
BM	1885 Hz	1737 Hz	1708 Hz	1777 Hz
GM	1975 Hz	1820 Hz	1755 Hz	1850 Hz

4.3.2 Chip analysis

When analyzing the collected chips, measured values for e_2 and h_2 were used together with *Equation 10* to obtain the segmentation distances. The scattered values of e_2 and h_2 for each passage and material are provided in *Figure 61-Figure 62* below. *Figure 59* and *Figure 60* shows representative images of segmented chips under the microscope.
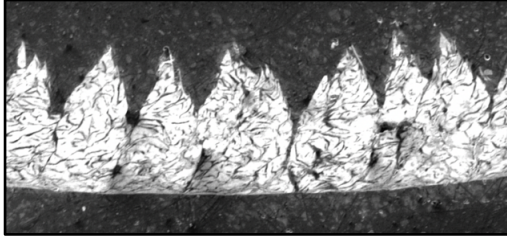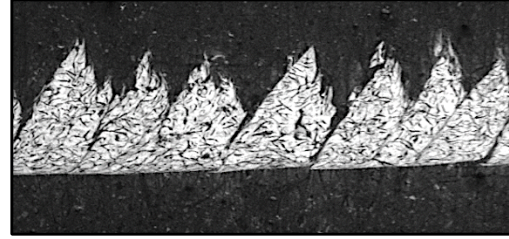
43

Figure 59. *Image of chip segments from BM.*

Figure 60. *Image of chip segments from GM.*

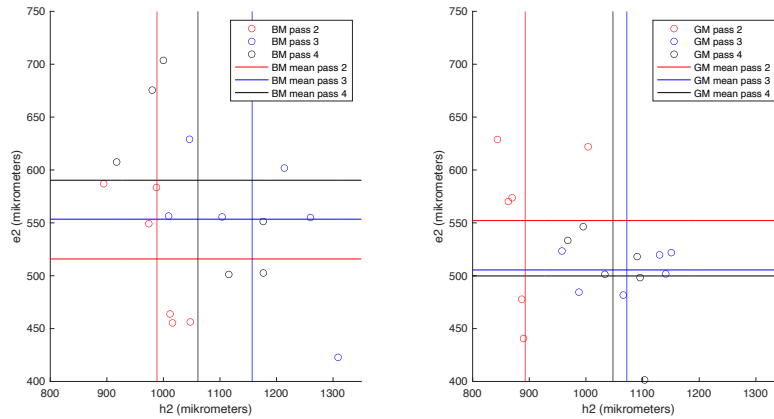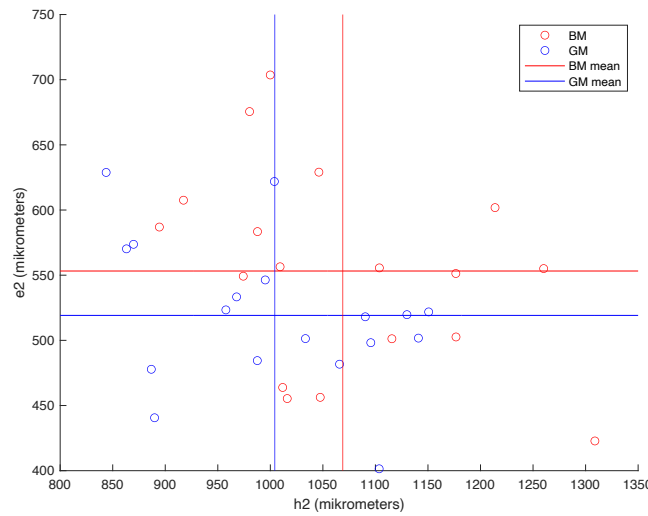**Figure 61**. *Measured values of chip geometry for all passages.*

Figure 62. *Chip geometry from both materials.*

The mean intersections in **Figure 61** and **Figure 62** were used to calculate the mean segmentation distance of each material. The values were then compared with the corresponding values from the cutting force analyses. The results are shown in **Figure 63**.
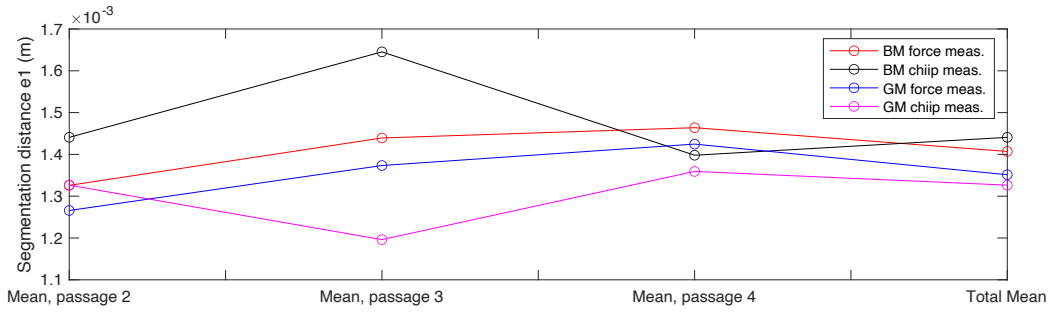
Figure 63. Segmentation distances from force and chip measurements.

4.4 Hardness analysis

Hardness measurement analyses generated a triple Weibull distribution for every measured direction. CDFs, PDFs, and every contributing distribution for direction 1 can be found in *Figure 64* and *Figure 65*. Corresponding data for the remaining directions can be found in *Appendix 2*.

Figure 66 shows comparisons between the two materials in each direction. It shows that in direction 1, GM has more pearlite. More hard particles were found in BM.

In direction 2 and 3, BM had more pearlite, but the pearlite in GM seemed to be harder. Again, more hard particles were present in BM.
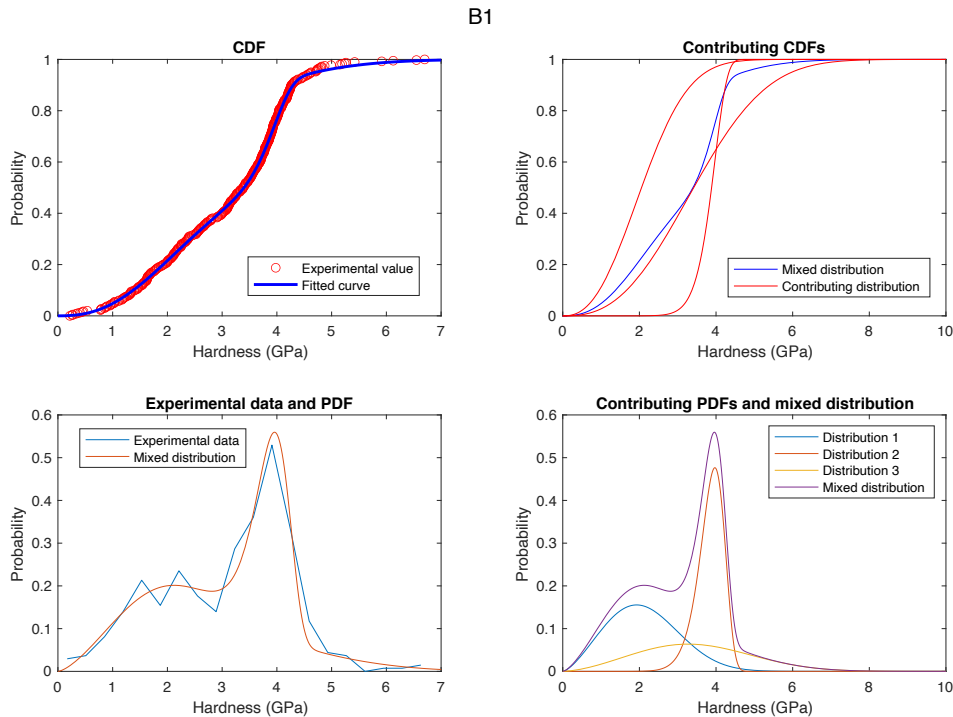

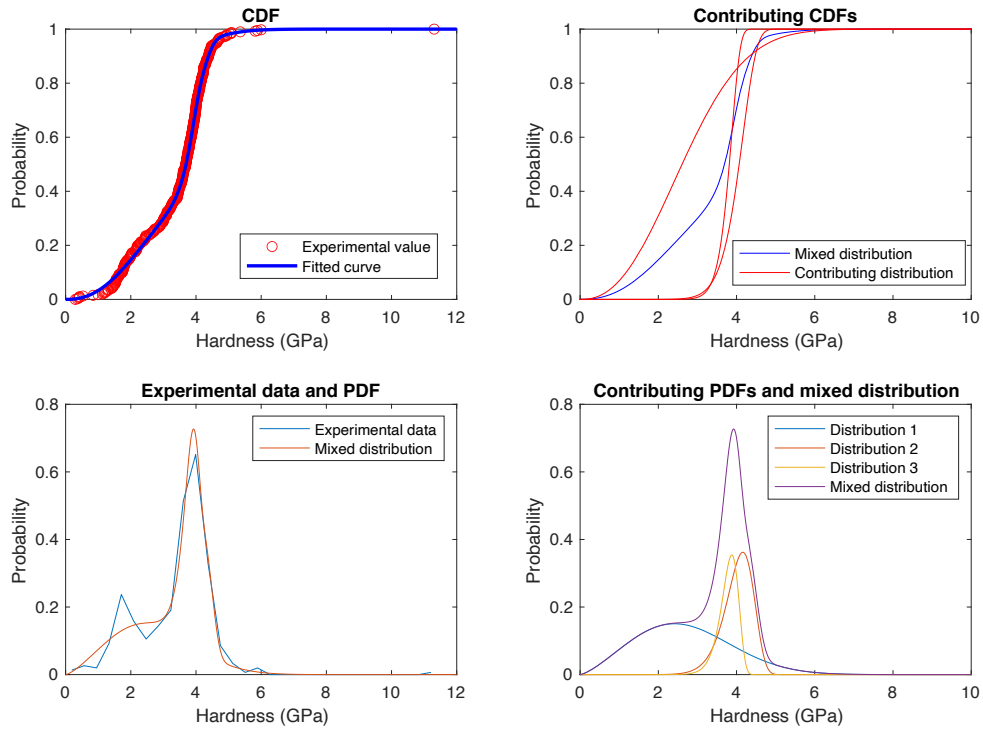*Figure 64.Hardness analysis for B1.*

G1

Figure 65. *Hardness analysis for G1.*

Stacking all directions from each material into two arrays and performing an overall hardness analysis generated the distributions found in ***Figure 67***. Here it is clear that BM had more soft phases and that GM had more pearlite. The pearlite in GM was also harder than the pearlite in BM. Once again, the hardest particles were found in BM. The mean hardness from every direction and the corresponding model errors can be found in ***Table 9*** and ***Table 10*** respectively.

Table 9. Mean hardness for all directions.

	B_1	B_2	B_3	B_{tot}	G_1	G_2	G_3	G_{tot}
Mean Hardness (GPa)	3.11	3.33	3.40	3.26	3.35	3.30	3.23	3.29

Table 10. *Model error of each hardness analysis.*

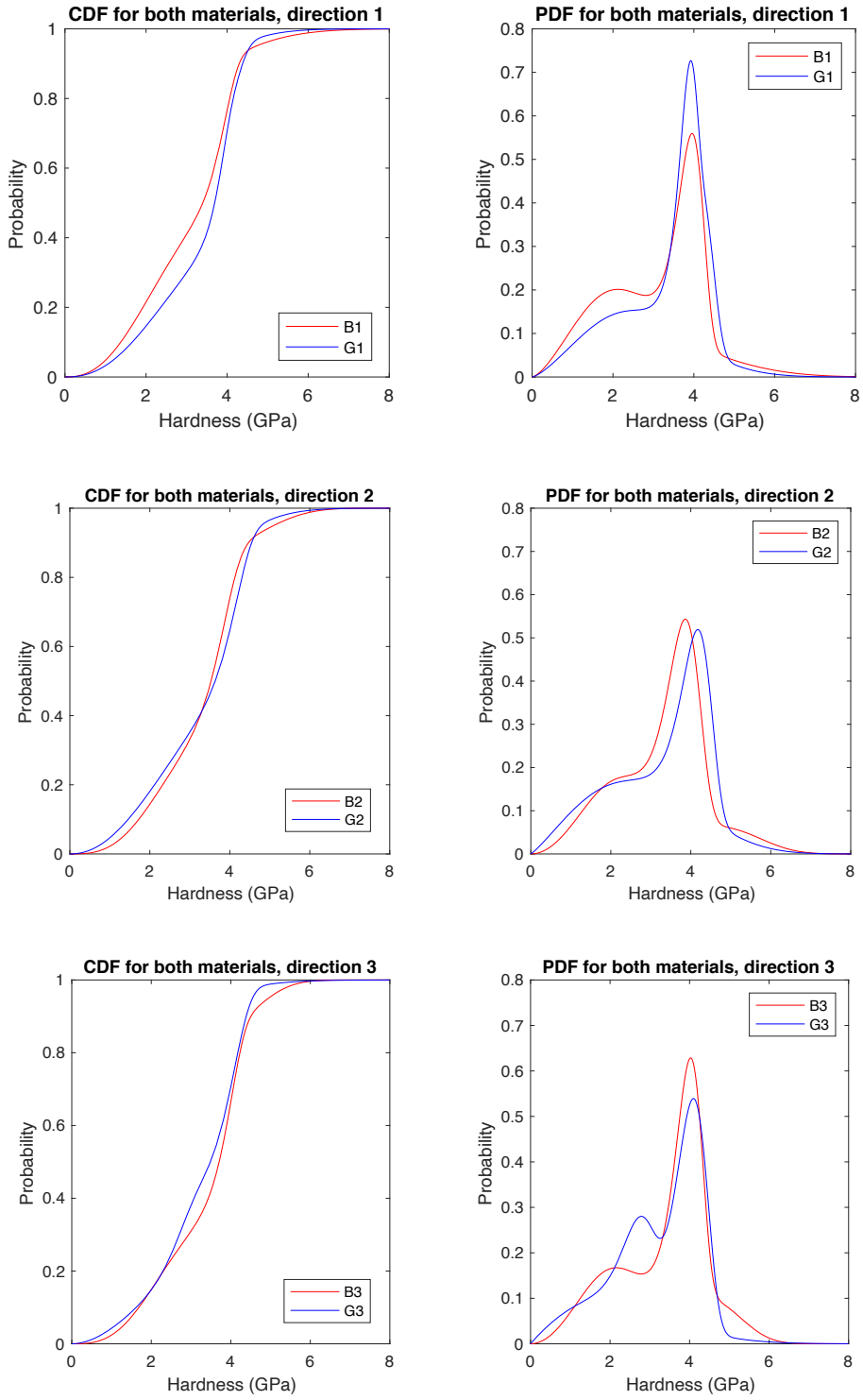|	B_1	B_2	B_3	B_{tot}	G_1	G_2	G_3	G_{tot}
ERR	0.44 %	0.64 %	0.47 %	0.30 %	0.68 %	0.48 %	0.47 %	0.30 %

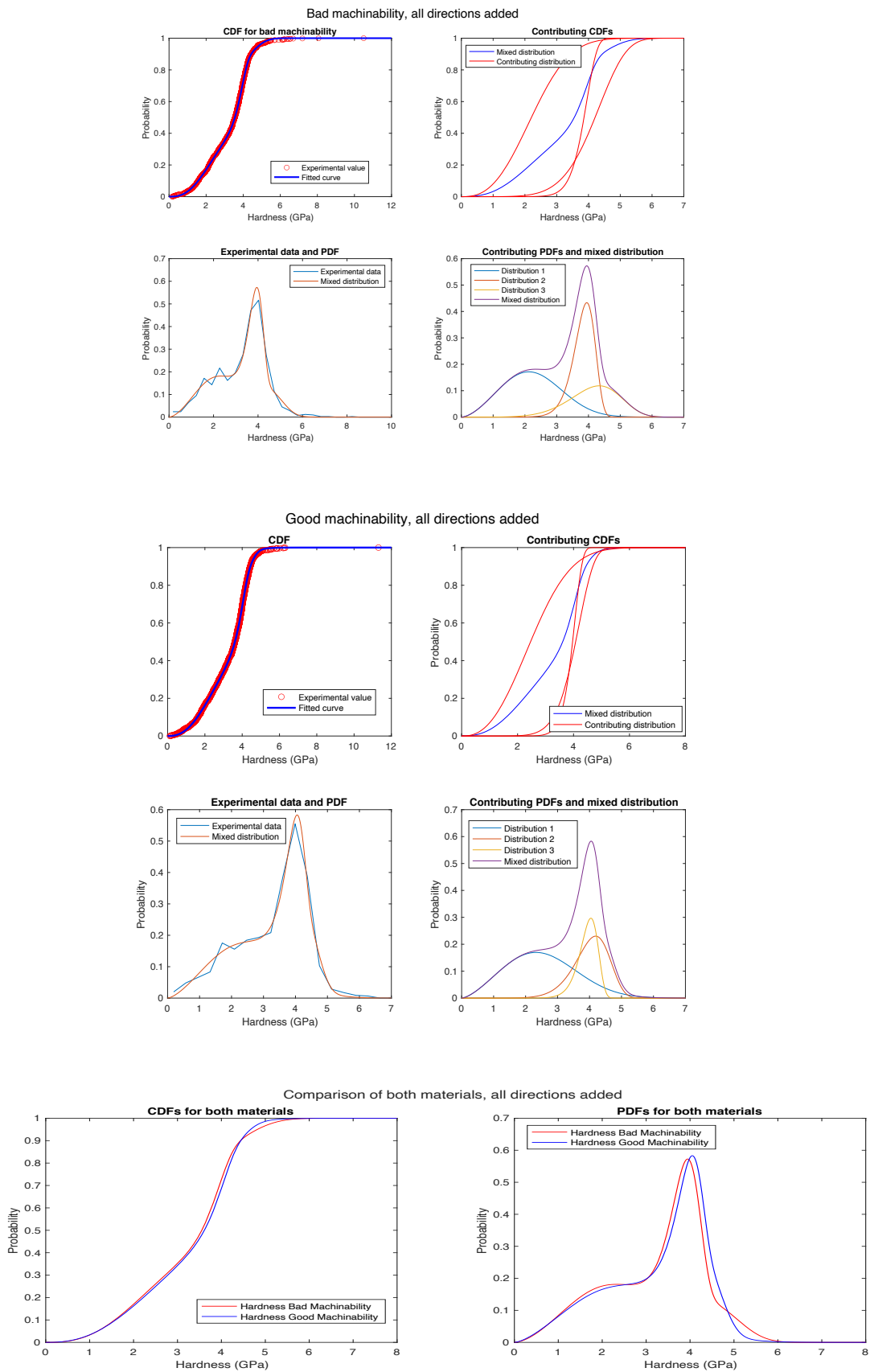***Figure 66**. Hardness comparison for each direction.*

***Figure 67**. Hardness analysis for both materials, all directions added.*

The samples from the hardness measurements were etched to identify the microstructures surrounding the indents. After a 20 second etching the indents were easily identified. The microstructures were however not distinguishable, which called for further etching. A 30 second etching was added, which led to distinguishable microstructures exemplified in *Figure 68* and *Figure 69*.
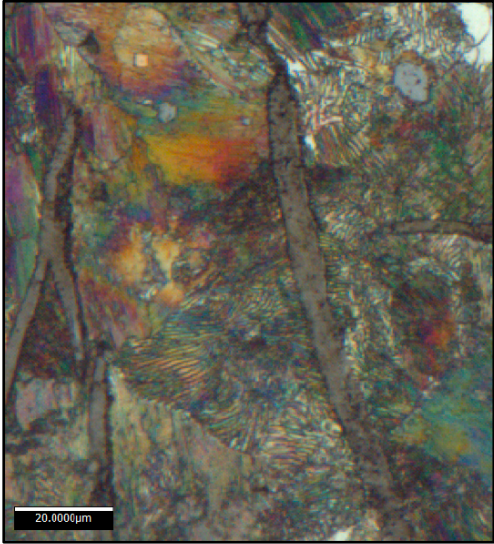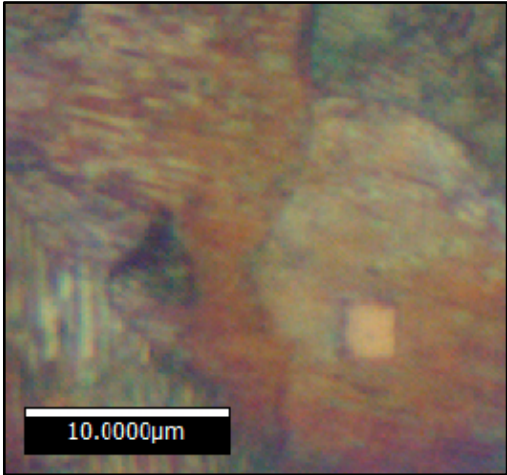

Figure 68. Grid pattern with 12 indents.

Figure 69. Indent in pearlitic structure.

Unfortunately, the indents were affected by the longer etching, making them hard to find in the samples. In addition, the grid patterns for the indents were affected by the etching with missing indents, making it hard to tie measured values to certain indents. Only 14 hardness values could be linked to microstructure, and these are found in *Table 11*. These show one indent in a hard steadite phase. The rest of the results show pearlite, or low hardness values where the indenter encountered both pearlite and graphite.

Table 11. Hardness and microstructure at distinguishable indents. P=pearlite, G=graphite, S=steadite.

Microstructure	S	P	P/G	P	P	P	P	P	P	P/G	P	P	P	P
Hardness (GPa)	5.41	4.15	1.30	3.18	3.29	4.24	4.54	5.11	4.75	2.46	2.34	3.52	4.26	3.85

4.5 Structure analysis

In this section, the results from the structure analyses are presented.

4.5.1 Graphite structure

Figure 71 and *Figure 72* shows representative images of the graphite structure of each disc. Each micrograph had an area of 1 mm^2. The material samples were divided into four zones of 2 mm depth each. Zone 1 represented the first millimeters below the friction plane surface, and zone 4 represented the core of the material. The zone locations are clarified in *Figure 70*.
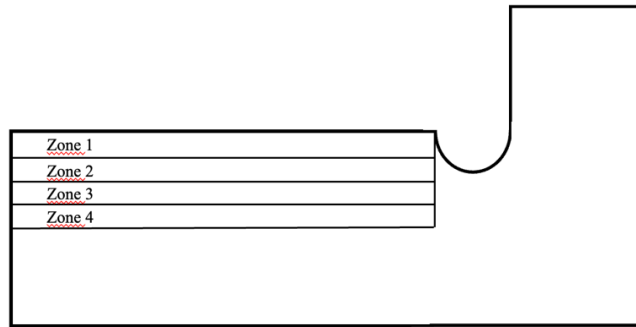
Figure 70. Principle cross sectional diagram illustrating depth zones in a brake disc.

As seen in ***Figure 71***, graphite form I was present throughout the material of BM. The distribution was predominantly made up of type A, with elements of type C. The size differed through the material, with graphite flakes growing with the depth. At zone 1, the sizes were 4 and 5. In zones 2-4 the sizes were mainly 1 and 2. In addition to this, flakes of sizes 5 and 6 were present throughout the material.

In GM, the form of the graphite flakes was of type I. The distribution was predominantly of type A, with elements of type C in this material as well. Again, the size of the flakes did grow with the depth of the material, with sizes 4 and 5 in zone 1 and sizes 3 and 4 in the remaining zones. Based on the graphite structure, the majority of the material in GM seemed to be harder than the material in BM. However, there were patches of smaller graphite flakes inside BM, indicating regions of increased hardness.
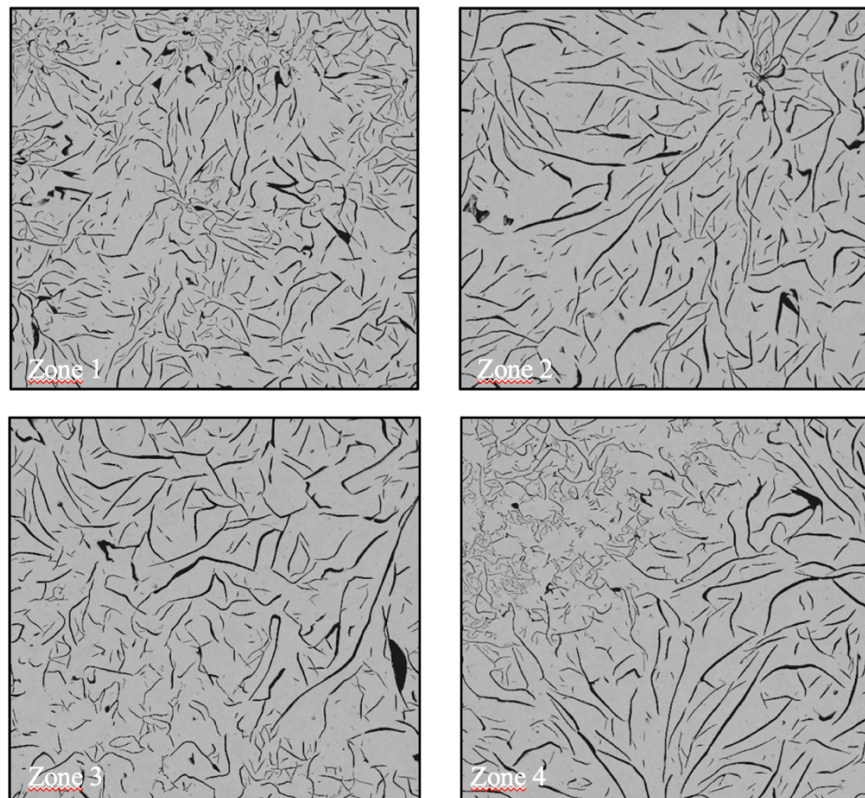
Figure 71. Graphite distribution in BM. Each micrograph has an area of 1mm².
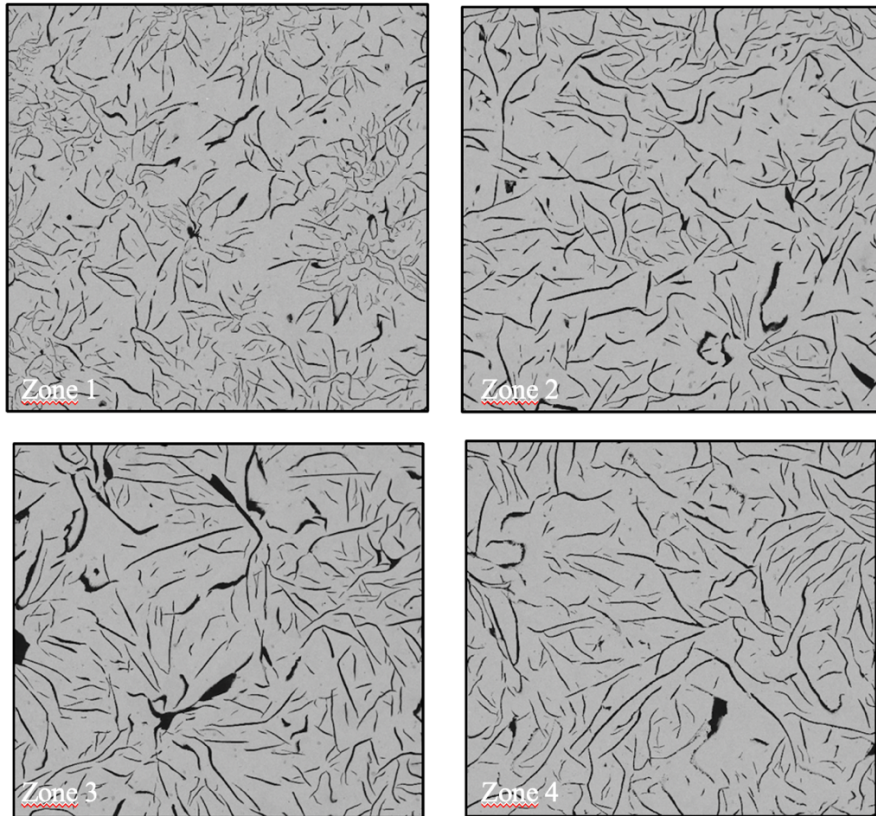
Figure 72. Graphite distribution in GM. Each micrograph has an area of 1mm².

4.5.2 Microstructure

Figure 73 and **Figure 74** show representative microstructures of mainly pearlite and graphite for both materials. Each micrograph has an area of 1 mm².
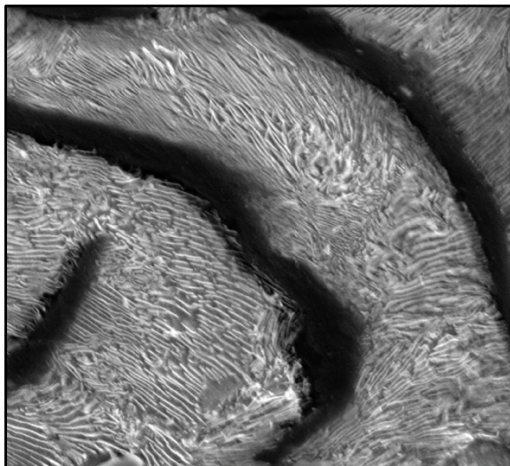
Figure 73. Microstructure of zone 1 for BM
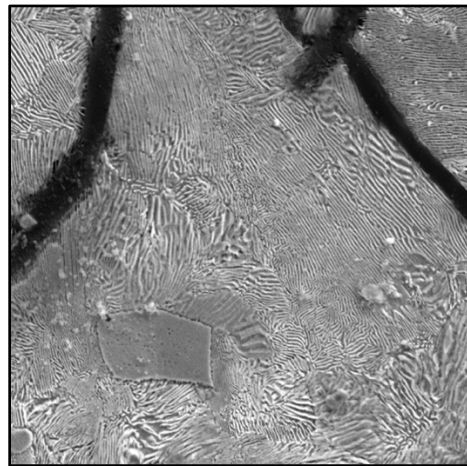
Figure 74. Microstructure of zone 1 for GM.

In search for free ferrite, regions resembling the one in **Figure 75** was observed. In GM, these regions often turned out to be steadite. 20 regions of interest were investigated in BM and 33 regions were investigated in GM. The difference in the number of observed regions was due to that more interesting regions were encountered in GM. The results can be found in **Figure 76**.
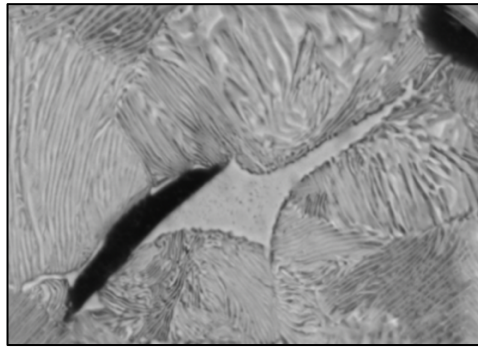
Figure 75. *Region of interest when looking for free ferrite.*
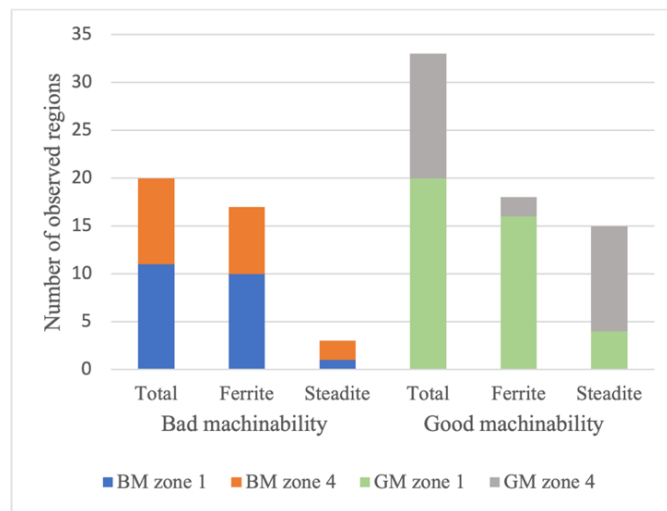
Figure 76. *Ferrite and steadite encountered in XEDS analysis.*

No free cementite was found in the XEDS-analysis, and all observed regions of free ferrite had an approximate diameter of 5-15μm. An approximation of the ferrite content based on size and encountered regions led to a content less than 1 %. Therefore, no microstructure quantification of the material matrix was performed, since there was no doubt that the material specification was fulfilled.

4.5.3 Inclusions

When analyzing the inclusion content, zones 1 and 4 were observed in each material. XEDS element mapping was performed, and 22 micrographs were generated for BM, and 23 micrographs were generated for GM. The results are found in ***Figure 77***. It shows that 90 % of all observed inclusions in BM were manganese sulfides. The remaining 9.8 % of the inclusions were carbides or nitrides. For GM, 76 % of all observed inclusions were manganese sulfides, with a remaining 23.9 % of hard inclusions.
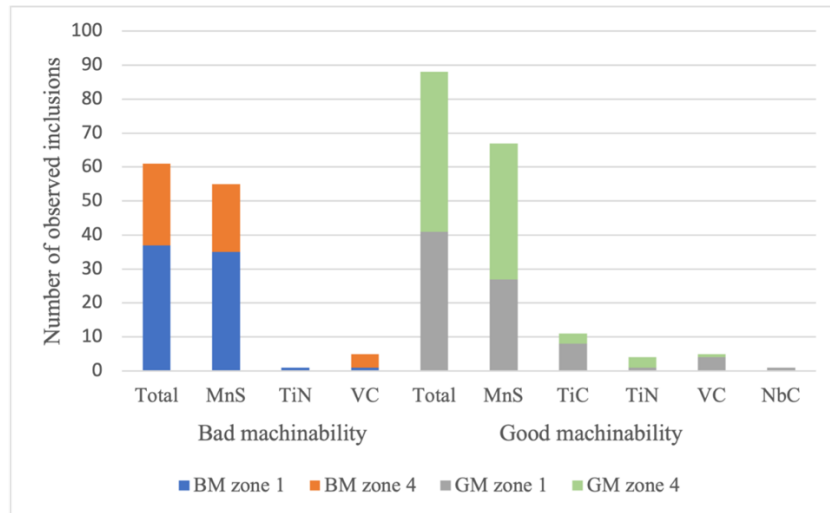
Figure 77. Observed inclusions in zones 1 & 4 for both materials.

4.5.3.1 Cast surface

To see if trace elements from the casting mold could constitute a machinability factor, the surfaces of the brake discs were investigated. Along the surface of BM, a total two grains of silica (SiO_2) were found along approximately 8 mm of the surface, see ***Figure 78***. Otherwise, the surface had a clean appearance with a thin graphite free layer, indicating a somewhat harder surface.
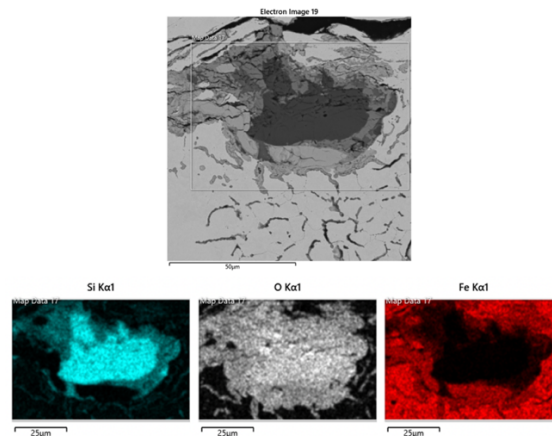
Figure 78. Silica found just below the surface of BM.

Along the surface of GM, four grains of silica were observed. Here too, the surface was graphite free, but with MnS-inclusions scattered in the material matrix, see ***Figure 79***. This could indicate a somewhat smoother machining process at the surface.
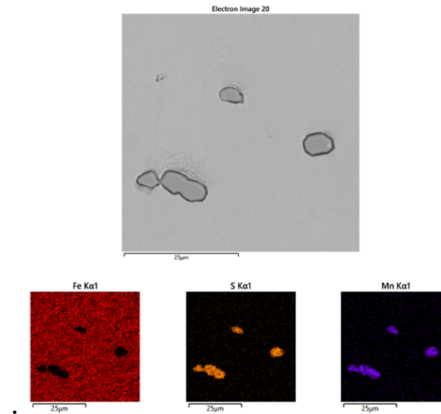
Figure 79. *MnS found just below the surface of GM.*

4.5.4 Grain size

The average grain size was measured in zone 1 and zone 4 for each material. Five micrographs from each zone were investigated and two lines were drawn in each micrograph. That resulted in an average based on 10 measured values per zone, i.e., 20 values per material. The interpretation of the micrographs was that grain boundaries occurred where the lamellae of pearlite changed direction. The results can be found in *Table 12*.

Table 12. *Average interpreted grain size of pearlite.*

	Avg grain size Zone 1 (μm)	Avg grain size Zone 4 (μm)	Avg grain size Tot (μm)
BM	11.9	15.3	13.6
GM	8.6	9.3	8.95

4.5.5 Chip analysis

When investigating the deformation zones of the chip segments, cracked steadite was found. Two chips from each passage, containing approximately ten segments each were observed for each material. A representative micrograph with element mapping can be found in *Figure 80*. The observed steadite regions were divided by size and depth in the material, and *Figure 81* shows that the concentration of cracked steadite was particularly big in GM. Concentrations were larger closer to the surface in GM, and closer to the core in BM.

Figure 80. *Chip from disc with good machinability, with cracked steadite in the deformation zone.*
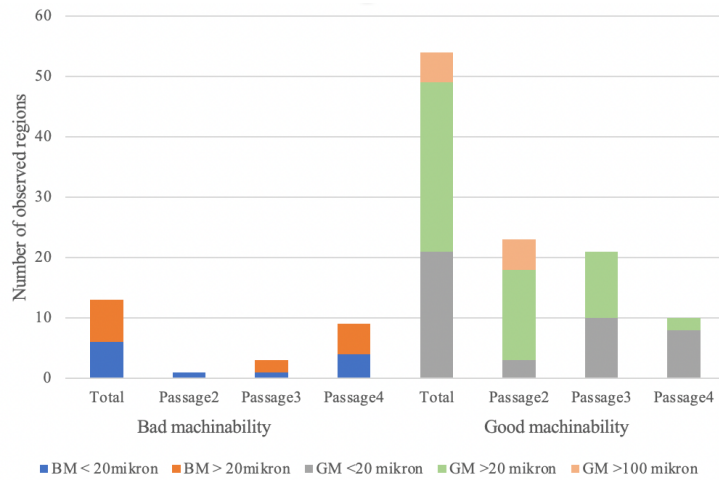
Figure 81. Regions of cracked steadite in chip deformation zone.

4.6 Cutting data optimization

Cutting data from **Table 2** was compared to recommendations from the manufacturer, found in **Table 13**. Recommendation for tool grade SL500 for OP50 were not consistent when comparing the company's catalogue and website. However, the website did not specify rough or fine turning for this specific grade, which the catalogue did. Recomm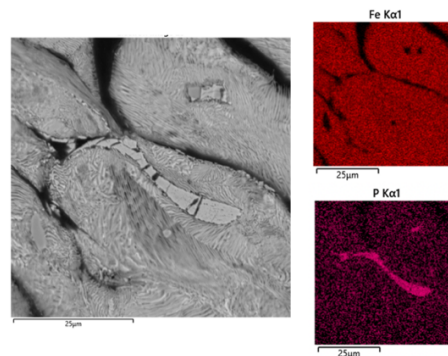endations for grade WBN 115 for OP20 and OP30 were consistent on both webpage and catalogue but did not specify kind of operation.

Table 13. Cutting data recommendations from manufacturer.

Source	Operation according to manufacturer	Tool grade	Cutting speed v_c (m/min)		Cutting depth a_p (mm)	Feed f (mm/rev)	
			Recomm. value	Overall range		Recomm. value	Overall range
CeramTec [29]	-	WBN 115	-	600-1800	0.25-4.0	-	0.1-0.7
CeramTec - website [30]	-	SL 500	-	400-1500	1.5-5.0	-	0.25-0.9
CeramTec - catalog [9]	Finishing	SL 500	900	400-1200	0.5-2.0	0.25	0.15-0.5

When comparing cutting data for OP20 and OP30, the values of speed and cutting depth are within range, but the feeds are above the recommended limits in both cases.

For OP50, the speed is above the recommended value but within the overall range. The cutting depth is just slightly below the recommended range and the feed rate exceeds the highest value for the recommended range for finishing operations.

5 Discussion

It is widely documented that cutting forces increase with tool wear. Since the machining tests did not last very long, no such observations were possible, and no substantial tool wear could be documented. Instead, the segmentation frequencies and the load functions from the force measurements were observed together with the chip measurements.

5.1 Machining tests

The analyses of the cutting forces and chip segments both showed a higher segmentation frequency for GM. Since the relative machinability of the two discs was known, the outcome of the frequency analysis confirmed the theory of better machinability as a result of increased segmentation frequency.

When comparing segmentation distances from *Figure 63*, the distances obtained from the cutting force analyses follow a clear trend, where segmentation distance increase slightly with the material depth. The calculated distances from chip measurements do not seem to follow any trend, and the values for passage 3 deviate substantially from the cutting force values. The mean segmentation distances from chip measurements do however approach values close to the ones obtained from the cutting force analyses.

The fact that the cutting speed decreased along each passage, which was neglected, could have an impact on the distance calculations of the chips. While the frequency analysis of the cutting forces generated a mean value for the entire steady state phase of each passage, the same procedure was not possible with the chips. The collected chips from each passage piled up during the machining tests, and it was not possible to know when in the process the analyzed chips were sheared off, i.e., at what cutting speed the chips were collected.

The deviating segmentation distances could also be explained by the fact that mounting and measuring the chips is a difficult task. It is hard to know if the chips were mounted at the right angle, if the polishing depth was correct, and if the interpretation of the chip geometry was satisfactory. Therefore, in this case, results should be used as a mere indication of the segmentation distance.

The relative size of the segmentation distances between the materials are confirmed in *Figure 52* and *Figure 53*. The wider distribution of forces together with a constant cutting speed indicate a longer segmentation distance for BM, granted that the cutting forces and resistance increase with the penetration depth of the tool.

When comparing *Table 7*-*Table 9* one can see that the load functions were consistently higher for BM, and the lowest value for BM exceeded the highest value for GM. This indicates that the load generated when turning BM was to a considerable amount distributed on the clearance face of the tool, probably due to a longer contact length. The high feed forces on the clearance face could indicate low temperatures in the tertiary shear zone, which eventually might lead to adhesive wear and BUEs. The cutting data does however influence the temperature, and the load function values should in this case be considered as an indication of relative machinability, rather than being used to identify wear mechanisms.

5.2 Hardness

The distribution of the pearlitic hardness values in *Table 11* confirms that pearlite can have hardness values within a wide range. In addition, these values correspond well to the assumed pearlitic distribution of the statistical model.

The hardness in direction 1 corresponds to the direction of the feed forces, and direction 2 corresponds to the main cutting forces. No correlation could be found between the directional hardness and the cutting forces when comparing *Table 6* and *Table 9*. However, when looking at the PDFs for the directional hardness, G_1 was clearly harder than B_1.

When comparing the PDFs of B_2 and G_2, the hardness varied through the materials. G_2 had less pearlite than B_2, but the pearlite in G_2 was harder. This indicates that the pearlite in B_2 was softer due to the amount of ferrite inside the microstructure lamellae. Still, B_2 had a higher mean hardness than G_2, while G_2 had better machinability.

The mean hardness for BM was higher in direction 3 as well, while the pearlite was slightly harder in GM, as seen in *Figure 66*. These observations could indicate that microstructural proportions should not be the only thing of interest when observing machinability. The individual properties of the present microstructures should also be investigated.

During a machining operation, a volume of material is removed with shearing in several directions. Therefore, it is assumed that the total hardness should be considered the most important aspect of hardness. The total hardness in *Figure 67* shows that GM had harder pearlite, more pearlite, higher mean hardness, and less soft phases than BM. GM was continuously harder than BM, with the exception that BM had a higher concentration of the hardest particles. These results are however contradictory to the results from the structure analysis, where the most carbides and nitrides were found in GM. This could indicate that BM might have wider pearlite lamellae, causing the indenter to occasionally interact with just cementite when in contact with pearlite. The hardness relation between the materials is confirmed by the grain size estimation, where the grains in GM were smaller. These results and the known relative machinability of the two discs indicate that high total hardness in general and high pearlitic hardness in particular could correlate to good machinability.

The hardness measurements have not been compared to the hardness requirements from the material specification. This since results from a nano indenter can only be compared to measurements made with the same load and the same indenter and cannot be compared to macro hardness. Besides this, the relative hardness between the materials was the focus for this study.

5.3 Structure analysis

The specification in *Table 1* shows the allowed amounts of constituents in the brake discs. In comparison with *Table 3* and *Table 4* the following can be concluded:

- The silicon content in GM is 0.01 % too low.
- None of the materials have enough copper. GM has the least copper.
- The materials have the same amount of chrome, but they do not have enough of it.
- GM has 0.001% more titanium and 0.01 more tin than BM. There are no titanium or tin limits in the specification.

Apart from what is stated above, the chemical compositions of the two materials are similar. However, the compositions do not seem to reflect the inclusion content found in the materials. GM do have more titanium, but only by a small amount, and no records of vanadium or niobium are found in the composition analyses or the specification.

According to *Table 3* and *Table 4*, both materials contain the same amount of Phosphorus. Despite this, much more steadite was found in GM, see *Figure 76* and *Figure 81*. Steadite in appropriate amounts appears to improve machinability, since much more cracked steadite was found in the chips of GM. A possible explanation to this behavior could be that the hard steadite regions could act as a fracture indicator facilitating chip breaking and chip segmentation. Another explanation could be that the possible voids originated from steadite solidification could act as chip breakers, improving machinability in the same manner as graphite does.

When searching for inclusions, MnS was clearly the most common sort, see ***Figure 77***. More MnS inclusions were found in BM, while more carbides and hard inclusions were found in GM. MnS has been proven to decrease the contact length and lubricate the cutting process. This can however not be confirmed from this analysis, since no contact length was measured, and a higher percentage of MnS inclusions were found in BM.

Carbides and other hard inclusions do not seem to hinder machinability if present in reasonable amounts. GM had the most carbides and nitrides, which are expected to act abrasive on the tool. This might be true, but the inclusions could also act as fracture indicators or weaken the material matrix as in the case with the steadite, improving chip breakage and segmentation when using a hard tool material like cBN. Another possible explanation could be that the amount of MnS in the material reduces the impact of hard inclusions.

Silicon inclusions have earlier been shown to improve machinability. This cannot be confirmed since no silicon inclusions were found and the compositions provided by ACF suggests a higher silicon content in BM.

An initial theory was that sand particles from the casting mold, or other trace elements on the brake disc surface could obstruct the machinability. This can however not be confirmed since no substantial amount of trace elements were found on the surface. In addition to this, it is clear that the machinability problems at ACF do not originate on the surface.

The discs were casted in April 2022 and the machining tests took place in October 2022. Since the main part of the age strengthening occurs within the first six to ten days after casting, machinability problems due to insufficient ageing can be excluded.

Graphite flakes of sizes 5 and 6 were present in patches through BM, indicating a hard structure. But the surrounding flakes were very big, larger than in GM. This could mean that BM is somewhat soft with hard zones scattered throughout the material. This might lead to cyclic loads, resembling intermittent cutting, causing fatigue problems on the tool. GM, on the other hand, had a more uniform graphite structure, with somewhat smaller flakes near the surface.

5.4 Cutting data optimization

The problems on production line 5 at ACF do not seem to originate on the surface, since inserts from OP20 had the least amount of wear. There were adhered layers present, but less than in the following stations. It is likely that the BULs from OP20 act protective on the cutting edge since the observed flank wear was modest. This further confirms that casting mold residue on the surface probably is not a problem. Especially when considering the hardness of the cBN inserts compared to the hardness of SiO_2.

Inserts from OP30 clearly had the most aggressive wear pattern. Excessive flank wear and crater wear were observed on every insert, and adhered material was found both inside and around the wear land. The crater wear in ***Figure 39*** could be a result of abrasive wear. However, the aggressive cutting data in ***Table 2****,* the hardness of the inserts and the shape of the wear in ***Figure 40*** suggest chemical wear due to elevated temperatures. Because of the hardness of cBN, it is not likely that any excessive abrasive wear is present, and the rounded contours of the wear land in ***Figure 40*** are often a result of chemical wear. When abrasive wear is present, the contours of the striations are likely to have a sharper geometry. The assumption of elevated temperatures is backed up by the fact that plenty of BULs were observed, but no BUEs.

It is clear that the inserts wear at the highest rate at OP30, indicating that problems with tolerances and surface quality starts there.

The graphite structure in both materials indicate a harder structure at the surface of the materials. This is often the case with casted materials due to longer solidification times at the core of the material. This could be an explanation to why the least amount of wear was found in OP20, even though OP20 has a higher MRR.

To solve the machining problems at hand, it is advisable to implement incremental production development. Following Hägglund's advice, the cutting depth should be established first, based on the as-cast dimensions, the dimensions of the finished product and the number or turning stations at hand on the production line.

Thereafter an initial feed value is set, maximized to increase the MRR. However, since the feed exceeded the recommended rates at every station, it is advisable to initiate lowered feeds in increments for evaluation. This does influence the production time negatively which should be taken into consideration. It has already been established that the recommendations from the manufacturer are not always reliable, since they often are adapted to a wide range of materials. They may however function as an indication of initial values when starting incremental production development and could suggest if one should increase or decrease the data in forthcoming increments.

Finally, an initial value of the cutting speed is set. Then the outcome of the parameters is evaluated as the production rate and quality has stabilized.

One suggestion is to observe the outcome of an increased cutting speed in OP30, to imitate the conditions in OP20, where wear is far less excessive. *Figure 28* suggests that an increase in cutting speed can have positive effects, even when cutting data is already high. This does however just concern the flank wear, and the adhesive and chemical wear might benefit from lower temperatures caused by a slower rotation. Still, an increased cutting speed at OP30 would be well within range of the manufacturer's recommendations. This would not affect the production time but could hopefully improve surface quality and tool life.

OP50 also seem to have a problem with adhered workpiece material. This was the only wear mechanism that could be identified since the adhered material on the inserts obstructed any flank wear measurements. It is assumed that the adhesion originates from elevated temperatures, since no BUEs were found and since OP50 used the highest cutting speed. OP50 also used a feed well over the recommended range for finishing operations. One might assume that the BULs could protect the cutting edge. However, since ACF reports that they experience a lot of tolerance problems at OP50, it is assumed that that the change in geometry caused by the BULs cause obstructions of surface quality.

If there is reason to believe that extensive chatter or poor surface quality is a problem caused by a segmentation frequency in the vicinity of the tool holders eigen frequency, there are measures to take. *Equation 12* suggests that the segmentation frequency alters with the cutting speed, so critical cutting speeds generating a chatter frequency do occur. Since a high segmentation frequency is desirable, it is advisable to increase the cutting speed if interfering frequencies are suspected. This holds if the increased speed stays within reasonable limits concerning other wear mechanisms. If not, the eigen frequency of the tool holder could be manipulated, or another tool holder might be considered.

An issue with this whole optimization approach is the fact that ACF experience machinability problems on a batch-basis, where one set of parameters that works on one specific batch has bad results on another batch. This might be solved by for example chip collection from each batch, where chip geometry is observed and cutting data is customized to avoid critical frequencies.

6 Conclusions

The conducted study affirms that machining behavior is a complex phenomenon that cannot be described or evaluated by a single measurement. The results of the study do however show interesting wear behavior and indicate certain desirable properties for machining applications. The conclusions below are divided into sections based on the three research questions.

6.1 Q1

Different wear mechanisms are expected on tools of different materials. The observed cBN tools showed signs of abrasive wear, chemical wear, and adhesion of workpiece material. The chemical wear was likely due to high temperatures in the cutting process. The ceramic tools only showed signs of having problems with adhesion, though the layer formations indicate that these tools were also subjected to elevated temperatures. No conclusions of tool wear due to the adhesion could be drawn, but the change in geometry caused by BULs could very well obstruct machinability and generate a poor product.

6.2 Q2

Table 14 shows a summation of the results of the machining tests. It can be concluded that load functions decrease with increased machinability. This while the segmentation frequency increase and the segmentation distance decrease. Also, when comparing similar materials, high hardness is desirable. Especially the hardness of the present pearlite. Hard inclusions do not seem to be a problem if there are lubricating inclusions present, or if the tool material is hard enough. Another conclusion is that the presence of steadite seem to improve chip breaking

Table 14. Summation of data.

	Bad Machinability	Good Machinability
Hardness (GPa)	3.26	3.29
Load function φ_{AT}	0.48	0.47
Segmentation frequency (Hz)	1777	1850
Segmentation distance (mm)	1.41	1.35
Grain size (μm)	13.6	8.95

For clarification of the conclusions, correlations of the results in ***Table 14*** and observations from the analyses can be found in ***Figure 82***.
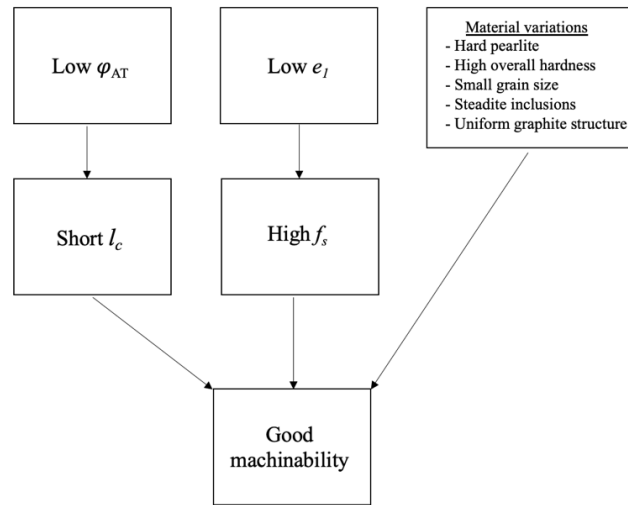
Low φ_{AT} | Low e_1 | Material variations
- Hard pearlite
- High overall hardness
- Small grain size
- Steadite inclusions
- Uniform graphite structure

Short l_c | High f_s

Good machinability

Figure 82*. Correlations of results.*

6.3 Q3

Recommendations for cutting data optimization were made, even though uncertainties of the outcome still exist. Since the machinability at ACF varies on a batch-to-batch basis, even when the batches come from the same supplier, the task of deciding a range of cutting data to implement on all batches on the line gets difficult. The possibility to analyze the materials in house on a batch basis is advisable if the quality of the castings continues to vary to the present extent.

6.4 Further work

To acquire further knowledge of GCI machinability, supplementary studies are recommended.

The performed tests should be repeated with additional hardness measurements on several depths, for comparison with the segmentation and microstructure at each respective depth. Also, structure analysis should be performed in three dimensions for comparison with the directional hardness.
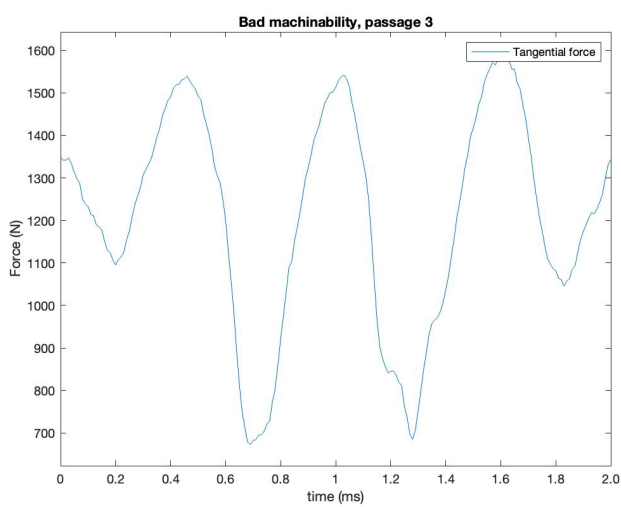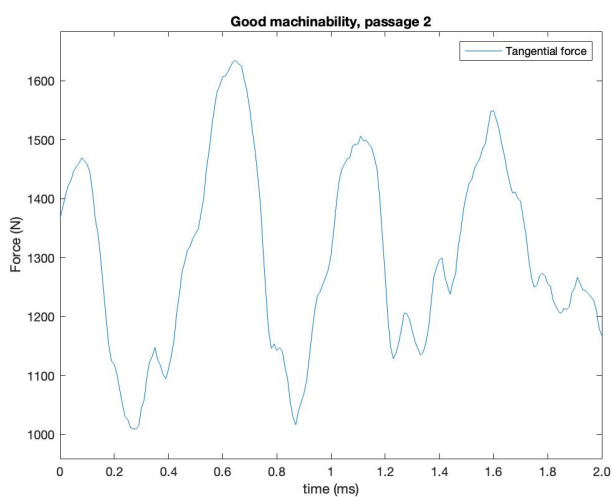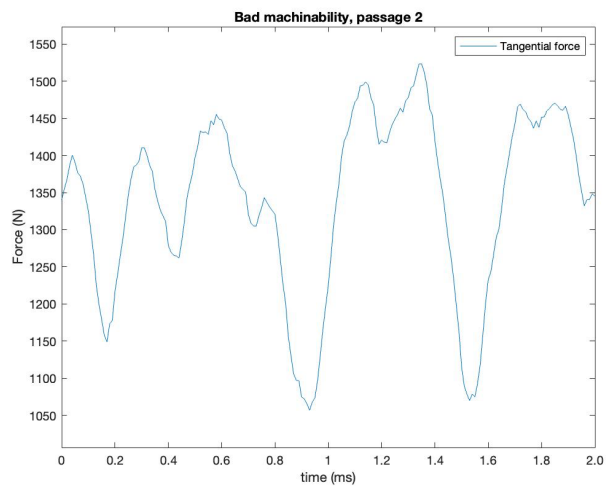
The amount of cracked steadite found in the chips from GM was not expected. Steadite in excessive amounts is assumed to be bad for machinability, but in this case the material with the most steadite had better machinability. Therefore, it would be interesting to study how steadite proportions in workpiece materials affect machinability.
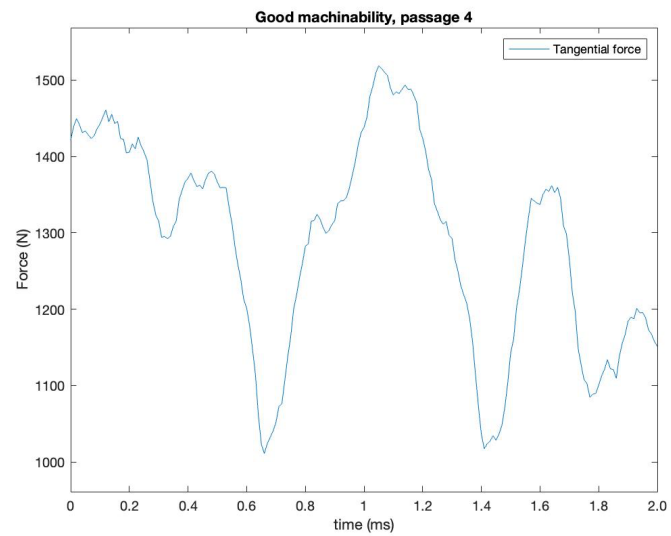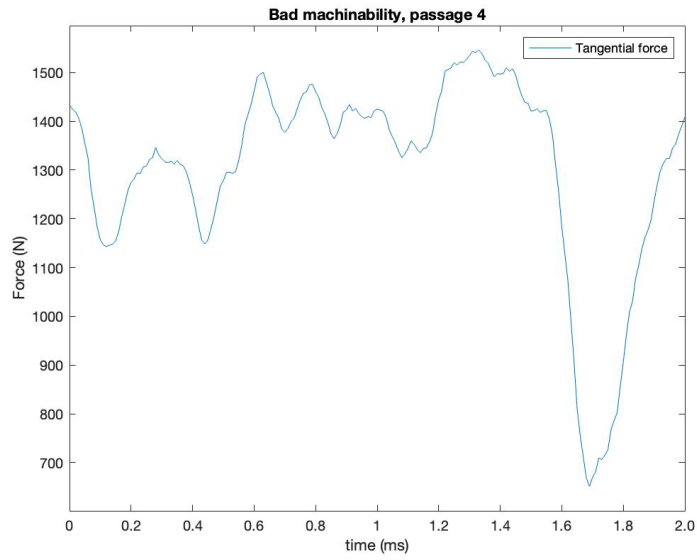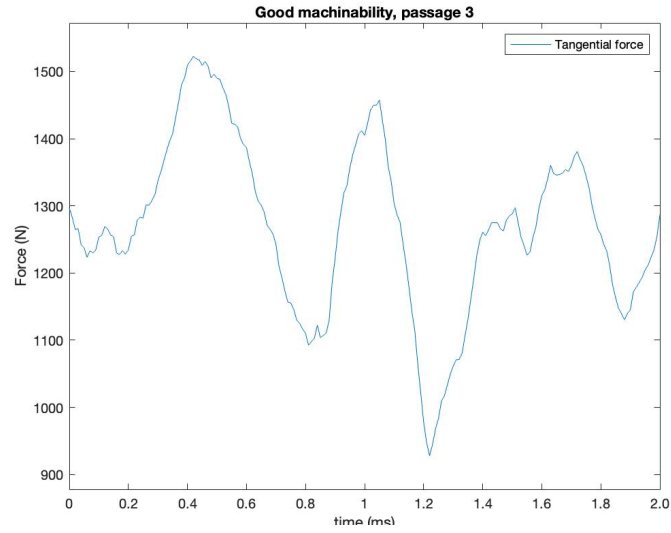
7 References

[1] J.-E. Ståhl, Metal Cutting - Theories and Models, Lund, Sweden: Seco Tools, 2012.

[2] E. M. Trent and P. K. Wright, Metal Cutting - Fourth Edition, Woburn MA, USA: Butterworth Heinemann, 2000.

[3] P. de Vos and J.-E. Ståhl, Metal Cutting - Theories in Practice, Lund-Fagersta, Sweden: Seco Tools AB, 2014.

[4] V. S. S. V. L. Sivaraman, "The Effect of Cutting Parameters on Cutting Force During Turning Multiphase Microalloyed Steel," *Procedia CIRP 4,* pp. 157-160, 2012.

[5] B. O. E. B. E. Aksu, "Analysis and Modeling of Edge Forces in Orthogonal Cutting," Faculty of Engineering and Natural Sciences, Sabanci University, Istanbul Turkey, 2008.

[6] A. Agic, "Analysis of Entry Phase in Intermittent Machining [Licentiate Thesis]," University West, Trollhättan, 2018.

[7] C. G. P. Scheffer, Practical Machinery Vibration Analysis and Predictive Maintenance, Burlington, MA: Newnes, 2004.

[8] A. Söderholm, "Variations in Material Properties of Grey Cast Iron and its Impact on Tool Wear," Division of Production and Materials Engineering, Lund University, Lund, 2021.

[9] CeramTec, *Ceramic Inserts - For Turning, Grooving and Milling,* Ebersbach/Fils, Germany: CeramTec, -.

[10] AB Sandvik Coromant, Modern Metal Cutting - A Practical Handbook, Sandviken, Sweden: AB Sandvik Coromant, 1994.

[11] International Standards Organization (ISO), *ISO 3865:1993 Tool-life testing with single-point turning tools,* Genève, Switzerland: International Standards Organization (ISO), 1993.

[12] L. C. Lee, K. S. Lee and C. S. Gan , "On the correlation between dynamic cutting force and tool wear," *International Journal of Machine Tools and Manufacture,* vol. 29, no. 3, pp. 295-303, 1989.

[13] G. F. Vander Voort, *ASM Handbook Volume 9: Metallography and Microstructures,* Materials Park OH, USA: ASM International, 2004.

[14] W. D. Callister and D. G. Rethwisch, *Materials Science and Engineering - An Integrated Approach, 5th Edition,* Hoboken NJ, USA: John Wiley & Sons, Inc., 2016.

[15] P. Schmidt, "Correlation between Solidification Time and Cooling Rate, Microstructure and Tensile Strength of a Low Alloyed Grey Cast Iron," Trans Tech Publications Ltd,, Switzerland, 2018.
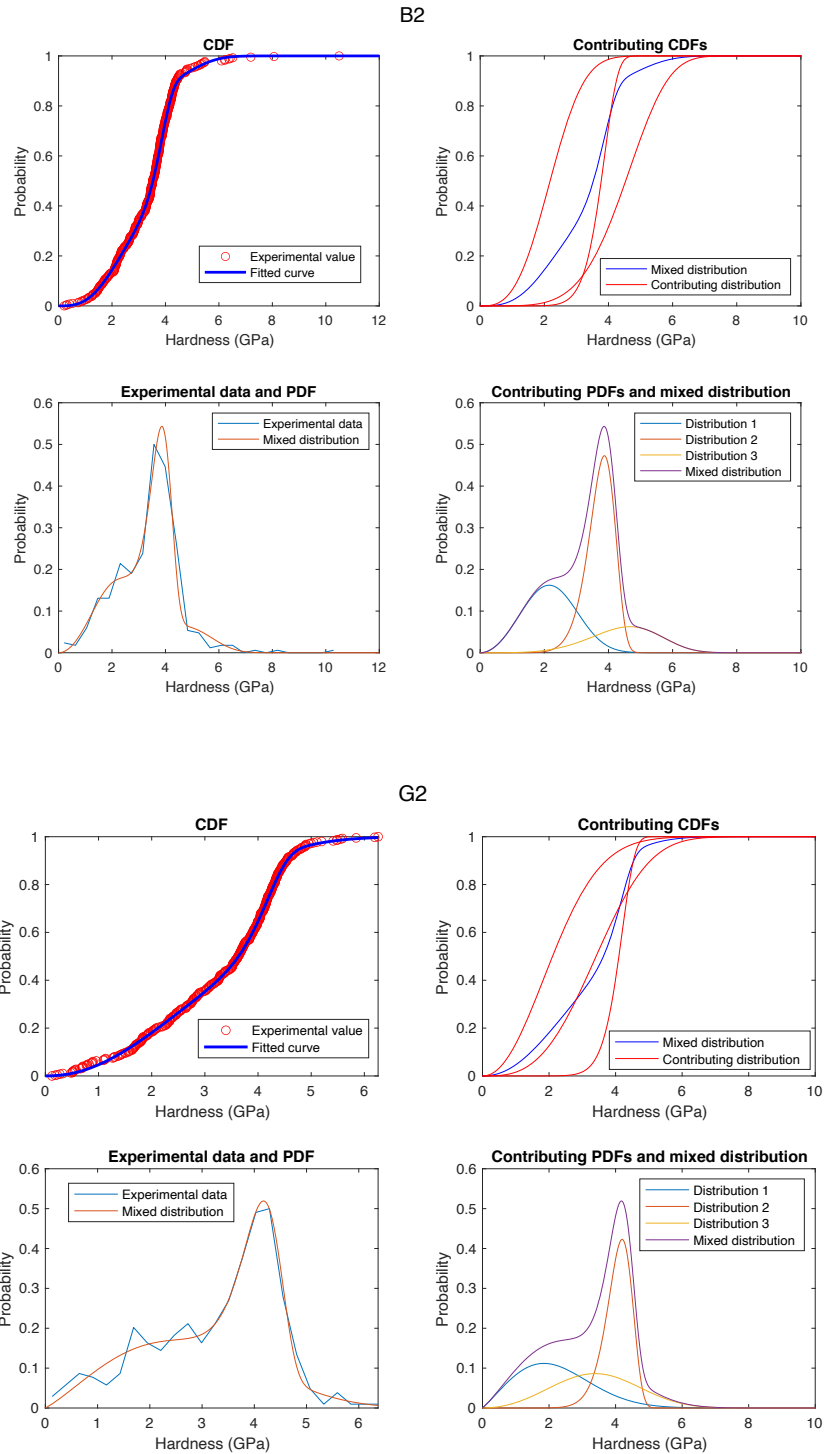
[16] M. Sahoo, "Microstructures of Cast Irons," in *Principles of Metal Casting, 3rd Edition*, McGraw Hill Education, 2014.

[17] P. Semih Genculu, *Cast Irons; Types, Properties, Applications & Weldability,* Fairfax VA, USA: PDH Online, 2015.

[18] R. Singh, Applied Welding Engineering: Processes, Codes and Standards, Amsterdam, Netherlands: Elsevier Inc., 2012.

[19] Swedish Standards Institute (SIS), *Microstructure Of Cast Irons - Part 1: Graphite classification by visual analysis (ISO 945-1:2008),* Stockholm, Sweden: SIS Förlag AB, 2008.

[20] W. Nicola and V. L. Richards, "Final Technical Report: Age Strengthening of Gray Cast Iron Phase III," Tri State University, Angola IN, USA, 2003.

[21] V. L. Richards, D. Van Aken and W. Nicola, "Age strengthening of gray cast iron," *International Journal of Cast Metals Research,* vol. 16, no. 1-3, pp. 275-280, 2016.

[22] S. N. Lekakh and V. L. Richards, "Aging and Machinability Interactions in Cast Iron," American Foundry Society, Schaumburg IL, USA, 2012.

[23] C. A. Schuh, "Nanoindentation studies of materials," *Materials Today,* vol. 9, no. 5, pp. 32-40, 2006.

[24] B. G. K. A. G. Kutchko, "Fly ash characterization by SEM–EDS," *Fuel,* vol. 85, pp. 2537-2544, 2006.

[25] J. E. Ståhl and C. Windmark, Sustainable Production Systems - The link between technology and economy with a global perspective, Lund, Sweden: -, 2021.

[26] S. Hägglund, "Methods and Models for Cutting Data Optimization [Doc. thesis]," Department of Materials and Manufacturing Technology, Chalmers University of Technology, Göteborg, 2013.

[27] R. Lindvall, "Cutting speed influence on machinability of gray cast iron flywheels - Competitive gray cast iron for sustainable development, Stage II," Division of Production and Materials Engineering, Lund University, Lund, 2019.

[28] Volvo Car Corporation, *Standard - Grey Iron,* 2008.

[29] CeramTec, "WBN 115," 2023. [Online]. Available: https://www.ceramtec-industrial.com/en/products-applications/machining-applications/cutting-materials/pcbn-cutting-materials/wbn-115. [Accessed 04 01 2023].

[30] CeramTec, "SL 500," 2023. [Online]. Available: https://www.ceramtec-industrial.com/en/products-applications/machining-applications/cutting-materials/silicon-nitride-ceramics/sl-500. [Accessed 04 01 2023].

[31] E. O. E. B. B. Aksu, "Analysis and Modeling of Edge Forces in Orthogonal Cutting," Faculty of Engineering and Natural Sciences, Sabanci University, Istanbul, Turkey, 2008.

Bad machinability, passage 2

Good machinability, passage 2

Bad machinability, passage 3

Good machinability, passage 3

Bad machinability, passage 4
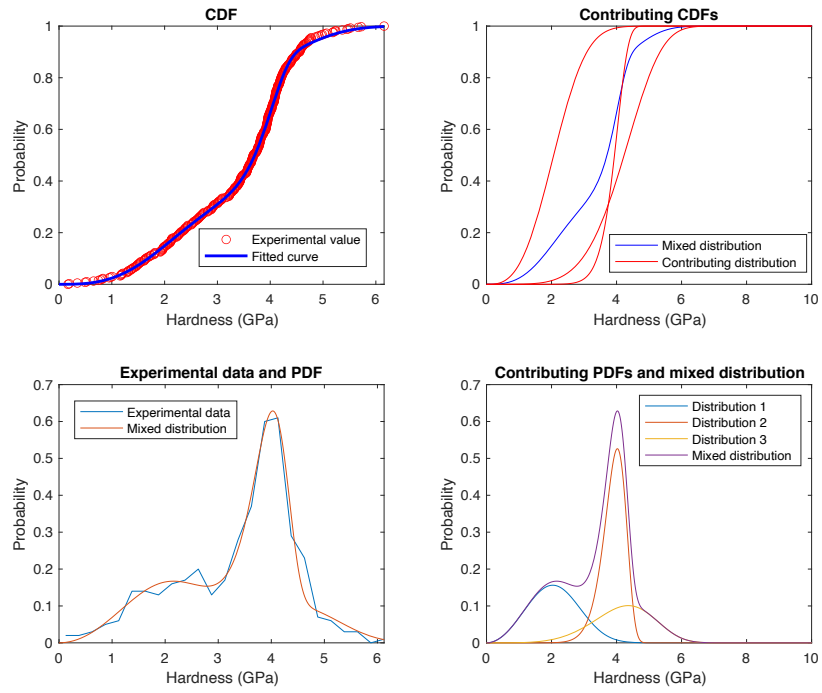

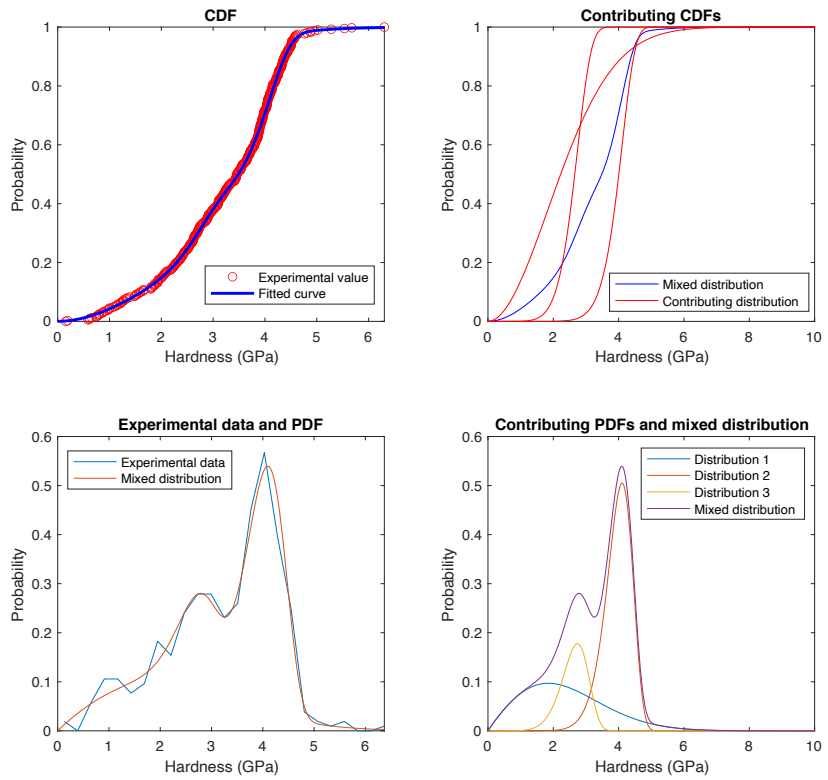### Good machinability, passage 4

65

Appendix 2. Hardness analysis

B2

G2

B3

G3

Appendix 3. Load functions